Matrix product state based band Lanczos solver for quantum cluster approaches

Sebastian Paeckel [1,*,†] Thomas Köhler [2,3,*,‡] Salvatore R. Manmana [4,§] and Benjamin Lenz [5,‖]

[1] *Department of Physics, Arnold Sommerfeld Center for Theoretical Physics (ASC), Munich Center for Quantum Science and Technology (MCQST), Ludwig-Maximilians-Universität München, 80333 München, Germany*

[2] *Department of Physics and Astronomy, Uppsala University, Box 516, S-751 20 Uppsala, Sweden*

[3] *SUPA, Institute of Photonics and Quantum Sciences, Heriot-Watt University, Edinburgh EH14 4AS, United Kingdom*

[4] *Institute for Theoretical Physics, Georg-August-University Göttingen, 37077 Göttingen, Germany*

[5] *IMPMC, Sorbonne Université, CNRS, MNHN, IRD, 4 place Jussieu, 75005 Paris, France*

(Received 15 November 2023; revised 21 September 2025; accepted 23 September 2025; published 2 December 2025)

We present a matrix-product state (MPS) based band Lanczos method as solver for quantum cluster methods such as the variational cluster approximation. While a naïve implementation of MPS as cluster solver would barely improve its range of applicability, we show that our approach makes it possible to treat cluster geometries well beyond the reach of exact diagonalization methods. The key modifications we introduce are a continuous energy truncation combined with a convergence criterion that is more robust against approximation errors introduced by the MPS representation and provides a bound to deviations in the resulting Green's function. The potential of the resulting cluster solver is demonstrated by computing the self-energy functional for the single-band Hubbard model at half filling in the strongly correlated regime, on different cluster geometries. Here, we find that only when treating large cluster sizes, observables can be extrapolated to the thermodynamic limit, which we demonstrate at the example of the staggered magnetization. Treating clusters sizes with up to 6×6 sites we obtain significant improvement over the extrapolation accessible with exact diagonalization solvers when comparing with quantum Monte Carlo results. Finally, we illustrate the applicability of the MPS cluster solver to more complex models by calculating spectral properties as relevant for the electron-doped cuprate $CaCuO_2$.

DOI: 10.1103/tjnr-kqmk

I. INTRODUCTION

Exploring the quantum states of matter of two-dimensional strongly correlated electron systems is inherently difficult. Prime examples are the cuprate high-temperature superconductors [1], whose salient features are frequently described within a single-band Hubbard-type model on a square lattice geometry [2–4]. More recently, two-dimensional materials have attracted substantial interest in a variety of systems, like bilayer graphene and other multilayered materials [5–7], transfer metal dichalcogenides (TMDCs) [8], or kagomé metals [9,10]. Experiments on these materials have revealed unconventional phases of matter, e.g., a Wigner crystal quantum Hall phase [11], or interesting superconducting phases [5–7,12–14], for which the role of flat bands and correlation effects is investigated. Hence, there is an urgent need to further develop numerical methods to treat two-dimensional (2D) systems.

Important progress in describing strongly correlated 2D systems has been achieved by the development of methods, which help to investigate quantum phases and quantum critical behavior directly in the thermodynamic limit. The fundamental insight is that the challenge of solving systems in the thermodynamic limit can be simplified by replacing it with an equivalent problem that is defined on a finite cluster, only. This is the foundation of so-called cluster-embedding techniques (CETs) such as dynamical mean-field theory (DMFT) [15–17], cluster-perturbation theory (CPT) [18,19], or variational cluster approximation (VCA) [20–23]. These approaches are often formulated in terms of Green's functions of the finite cluster and the embedding is defined such that the cluster Green's function describes best that of the actual physical system. Despite others, the success of these methods is based on the intimate relation between Green's functions and experimental observables, for instance spectral functions, which allows for the direct comparison between theory and experiment [24,25].

With the development of CETs, which contain the mapping of lattice problems to finite clusters, the focus has shifted to determine the cluster Green's function, which still constitutes a computational highly nontrivial problem. Important classes

*These authors contributed equally to this work.
†Contact author: sebastian.paeckel@physik.uni-muenchen.de
‡Contact author: t.kohler@hw.ac.uk
§Contact author: salvatore.manmana@theorie.physik.uni-goettingen.de
‖Contact author: benjamin.lenz@sorbonne-universite.fr

Published by the American Physical Society under the terms of the Creative Commons Attribution 4.0 International license. Further distribution of this work must maintain attribution to the author(s) and the published article's title, journal citation, and DOI.

of methods to approach this task are wave-function-based methods, like exact diagonalization (ED) [26,27] or tensor-network state (TNS) methods [28,29], and sampling-based methods, like quantum Monte Carlo (QMC) [30–32]. ED cluster solvers are conceptionally the most simple approach and despite the fact that an extreme degree of optimization has been achieved, incorporating various symmetries and exploiting massive parallelization [33], they suffer drastically from the exponential growth of the Hilbert space, limiting the practically doable number of cluster sites for single-band Hubbard models to $\approx O(20)$. On the other hand, TNSs realized as MPSs [34] are extremely successful in one dimension, but the area law of entanglement or the entanglement barrier in nonequilibrium situations highly limits their applicability to 2D systems [35]. From a quantum information perspective, finite projected entangled-pair states (PEPSs) [29,36] should be optimal. However, these algorithms have been shown to exhibit only extremely slow convergence for Hubbard-type systems [37]. Finally, QMC methods have their limitations due to the fermionic sign problem [38], which restricts the class of solvable cluster Hamiltonians.

In this paper, we introduce an efficient MPS-based scheme for calculating the cluster Green's function and apply it within the context of VCA. It turns out that a naïve treatment of established Krylov-based methods in a MPS framework would barely improve the range of applicability of the VCA. However, when combining the MPS with a band Lanczos scheme as well as an energy truncation, it is possible to treat cluster geometries well outside the reach of ED solvers and without principal limitations on the Hamiltonian.

The remainder of the paper is structured as follows: In Sec. II we introduce the single-band Hubbard model and the basic idea of cluster methods, such as the VCA. In Sec. III we discuss in detail our band Lanczos ansatz for MPS, including the energy truncation scheme, an error estimate using the Hochbruck-Lubich bound [39], a useful energy rescaling, and a discussion of the loss of orthogonality of the Lanczos vectors within the MPS framework. Furthermore, Sec. III B discusses further aspects of the VCA as relevant for this paper, and Sec. III C discusses our choice of clusters, including Betts clusters. Section IV presents the main results of this paper obtained with our band Lanczos MPS + VCA ansatz, including a detailed analysis of the scaling of the results with the MPS bond dimension and a comparison of the staggered magnetization after scaling to infinite cluster size with numerically exact QMC results, as well as results for the spectral function. We finish the results section by applying the band Lanczos MPS + VCA ansatz to calculate spectral properties of a more complex model as relevant to electron-doped $CaCuO_2$. In Sec. V we conclude and provide an outlook to further applications of our method. The Appendix presents technical details of the calculations.

II. MODEL AND NUMERICAL TECHNIQUE

The model for which we benchmark our solver is one of the most common ones to study strongly correlated electron systems in two dimensions, the one-band Hubbard model with nearest-neighbor hopping [40]. The corresponding Hamiltonian reads

$$\hat{H} = -t \sum_{\langle i,j\rangle,\sigma} (\hat{c}^\dagger_{i,\sigma}\hat{c}_{j,\sigma} + \text{H.c.}) + U \sum_i \hat{n}_{i,\uparrow}\hat{n}_{i,\downarrow}, \tag{1}$$

where $\hat{c}^{(\dagger)}_{j,\sigma}$ are the annihilation (creation) operators of electrons of spin σ and $\hat{n}_{j,\sigma} = \hat{c}^\dagger_{j,\sigma}\hat{c}_{j,\sigma}$ is the particle number operator for a given spin σ on site j.

For our band Lanczos solver we have quantum cluster techniques in mind, for which a finite-size scaling in cluster size is known to be notoriously difficult in 2D [3,4]. In particular embedding the cluster into an effective environment, various factors need to be considered, such as the ratio between cluster-bulk and cluster-boundary sites, the connectivity of boundary sites, or the cluster geometry. Given these complications, which we discuss in more detail in Sec. III C, the main goal of our band Lanczos solver is to provide a tool that can handle various cluster geometries while increasing the cluster sizes as much as possible. A prime example for a quantum cluster technique is CPT [18,19], which can be derived from strong-coupling perturbation theory [41,42], and which allows us to calculate the spectral function based on the cluster Green's function. In CPT, the lattice is tiled into a superlattice of—most of the time identical—clusters. The intercluster hopping terms are then collected into a matrix $\mathbf{V}$ and treated in lowest-order perturbation theory when constructing the CPT Green's function:

$$\mathbf{G}^{\text{CPT}}(\tilde{\mathbf{k}}, \omega) = [[\mathbf{G}^{\text{cluster}}(\omega)]^{-1} - \mathbf{V}(\tilde{\mathbf{k}})]^{-1}. \tag{2}$$

Here $\tilde{\mathbf{k}}$ are reduced wave vectors corresponding to the partial Fourier transform with respect to the superlattice vectors. In the following, we omit the superscript and refer to the cluster Green's function as $\mathbf{G}(\omega)$.

The error of the perturbative treatment within CPT is expected to reduce when enlarging the ratio of cluster "bulk" to cluster boundary, for instance when scaling up clusters of fixed geometry. In addition to the cluster size, different geometries allow us to precisely account for the spectral function at different wave vectors $\mathbf{k}$.

CPT has been used not only for model calculations on the Hubbard [19], tJ [43], and pure spin models [44] but also for more realistic modeling of materials, e.g., in the context of Mott insulators such as NiO [45] or (doped) cuprates [42,46–48]. It can also be extended to nonlocal interactions [49], electron-phonon coupling [50], nonequilibrium problems [51], or even be used to calculate two-particle responses [52]. CPT is thereby not only conceptually simple, but also one of the most versatile quantum cluster techniques.

However, CPT is limited in that it does not allow us to study symmetry-broken phases. An extension of the technique mends this deficiency by including symmetry-breaking Weiss fields on the cluster, which are determined according to a variational principle. The variational CPT, more commonly known as VCA [20,21], will be introduced in more detail in Sec. III B.

For benchmarking purposes, we add here a Weiss field term on the cluster corresponding to a staggered magnetic field,

$$\hat{\mathcal{H}}_{\text{AF}} = h_z \sum_l e^{i\mathbf{Q}\cdot\mathbf{R}_l}(\hat{n}_{\mathbf{R}_l,\uparrow} - \hat{n}_{\mathbf{R}_l,\downarrow}), \tag{3}$$

where l denotes cluster sites and the Néel ordering wave vector is $\mathbf{Q} = (\pi, \pi)$. A detailed VCA study of antiferromagnetism (AFM) in the 2D Hubbard model using this Weiss field can be found in Ref. [21]. For the following, it is important to note that the (cluster) Green's function of $\hat{H} + \hat{\mathcal{H}}_{\mathrm{AF}}$ needs to be determined.

III. METHOD

In this section we introduce the band Lanczos algorithm for calculating the cluster Green's function using MPSs. Several routes have been pursued so far to employ MPS-based cluster solvers for CET. This includes time-evolution-based solvers obtaining the cluster Green's function from real or in imaginary time evolution [53–57], expanding the resolvent in terms of orthogonal polynomials [58–60], reformulating the determination of the resolvent as optimization problem using correction vectors [61,62], or evaluating the Green's matrix elements explicitly by means of a global Lanzcos approach [63].

Nevertheless, despite each of these methods being considerably successful in the past, their applicability to VCA is rather limited. Standard time-evolution-based solvers require considerable system sizes to avoid too fast entanglement growth, due to reflections of excitations at the cluster boundary. Evaluating the resolvent in terms of orthogonal polynomials on the other hand, typically requires a large number $\approx\mathcal{O}(100)$ of basis states, each of which is obtained by applying the Hamiltonian to its predecessor, and thereby rapidly increases the state's entanglement. This limitation is partially overcome by a direct Lanczos expansion of each Green's matrix element, which typically requires only $\approx\mathcal{O}(10)$ applications of the Hamiltonian, per matrix element. However, a lot of information about the low-energy states is generated repeatedly, since each matrix element is constructed independently of every other. Furthermore, the reduced numerical precision using MPS arithmetics typically causes severe orthogonality problems after more than 10 applications of the Hamiltonian. The necessary application of further reorthogonalization techniques common to global Krylov methods [64] deteriorates the computational efficiency such that cluster sizes beyond those doable using exact methods can only hardly be reached.

In sight of these complications, the band Lanczos [65,66] offers a promising approach to evaluate the cluster Green's function in a global Krylov subspace representation, employing various initial states. In the following, we first summarize the general idea of the band Lanczos and introduce the necessary steps to obtain a meaningful convergence criterium. Afterwards, we recapitulate the necessary theory of the VCA, in order to use the band Lanczos algorithm as its cluster solver.

A. Band Lanczos with MPSs

The quantity of interest of most CETs is the cluster Green's function in frequency space, which can be written componentwise for electrons in real space as

$$G^{(e)}_{\mu\mu'}(\omega) = \langle\psi|\hat{c}_{\mu}(\hat{H} - E_0 - \omega)^{-1}\hat{c}^{\dagger}_{\mu'}|\psi\rangle, \tag{4}$$

where we combined site and spin labels into greek letters $\mu = (i, \sigma)$, $\mu' = (j, \sigma')$ and the superscript (e) indicates that here we are describing the electron part. The cluster Green's function for holes, indicated by a superscript (h), can be written in a similar manner by exchanging the creation and annihilation operators and replacing $\omega \to -\omega$. In the band Lanczos method, the Green's function is calculated by constructing a Krylov subspace using several electron and hole excitations, which serve as initial states. Representing the initial states as MPSs and the Hamiltonian as a matrix-product operator (MPO), the Krylov subspace construction can be performed in principle using standard MPS arithmetics. The particular choice of the set of initial states can depend on the cluster symmetries, but for the sake of simplicity we restrict ourselves in the following to the simplest case and ignore symmetries.

Consider the ground state $|\psi\rangle$ of a cluster, given by the Hamiltonian $\hat{H}$ acting on $L \in \mathbb{N}$ cluster sites, where each site j can host electronic degrees of freedom described by annihilation (creation) operators $\hat{c}^{(\dagger)}_{j,\sigma}$. We define a set of initial states $|\varphi^{(e)}_{j,\sigma}\rangle = \hat{c}^{\dagger}_{j,\sigma}|\psi\rangle$ and introduce the spin σ electron Krylov subspace $\mathcal{K}^D_{\sigma}$ with $D = NL$, generated from $N-1$ applications of $\hat{H}$ to the L initial states with spin σ:

$$\mathcal{K}^0_{\sigma} = \mathrm{span}\left\{\left|\varphi^{(e)}_{1,\sigma}\right\rangle, \ldots, \left|\varphi^{(e)}_{L,\sigma}\right\rangle\right\}, \tag{5}$$

$$\mathcal{K}^D_{\sigma} = \mathcal{K}^{D-1}_{\sigma} \cup \mathrm{span}\left\{\hat{H}^N\left|\varphi^{(e)}_{1,\sigma}\right\rangle, \ldots, \hat{H}^N\left|\varphi^{(e)}_{L,\sigma}\right\rangle\right\}. \tag{6}$$

Note that replacing the creation operators with the annihilation operators $\hat{c}^{\dagger}_{j,\sigma} \to \hat{c}_{j,\sigma}$, we obtain another set of initial states $|\varphi^{(h)}_{j,\sigma}\rangle = \hat{c}_{j,\sigma}|\psi\rangle$, from which we construct the spin σ hole Krylov subspace $\bar{\mathcal{K}}^D_{\sigma}$. For each Krylov subspace, an orthonormal basis is obtained from an iterative orthogonalization scheme. Thereby, given a set of orthogonal Krylov vectors $|k_{\alpha,\nu}\rangle \in \mathcal{K}^D_{\sigma}$ with $\alpha \in \{1, \ldots, \tilde{L}\}$ $(\tilde{L} \leqslant L)$ and $\nu \in \{0, \ldots, N-1\}$, a new set of candidate states $\{|k_{\alpha,N}\rangle\}$ is generated by applying the Hamiltonian to all states $\{|k_{\alpha,N-1}\rangle\}$. Just as in the conventional Lanczos scheme [67], every candidate state $|k_{\alpha,N}\rangle$ is then reorthogonalized against its $2L$ predecessors $|k_{\alpha,N-1}\rangle$ and $|k_{\alpha,N-2}\rangle$. Furthermore, candidate states have to be orthogonalized against each other, i.e., upon adding a new candidate state $|k_{\alpha,N}\rangle$, it needs to be orthogonalized against all $|k_{\alpha'<\alpha,N}\rangle$. It may occur that the states $|k_{\alpha,N}\rangle$ generated by this recursion are not linearly independent. This situation is typically solved by applying a so-called deflation scheme, reducing the range $\tilde{L}$ of the α's until all Krylov states $|k_{\alpha\leqslant\tilde{L},N}\rangle$ are linearly independent [65].

Following this strategy, a global Krylov basis is constructed that allows for a representation of the Green's function Eq. (4) in a Krylov subspace

$$G^{(e)}_{\mu\mu'}(\omega) \approx \sum_{\nu,\alpha_\nu}\sum_{\nu',\alpha'_{\nu'}} \langle\psi|\hat{c}_{\mu}\left|k_{\alpha_\nu,\nu}\right\rangle\left\langle k_{\alpha'_{\nu'},\nu'}\right|\hat{c}^{\dagger}_{\mu'}|\psi\rangle \times \left\langle k_{\alpha_\nu,\nu}\right|(\hat{H} - E_0 - \omega)^{-1}\left|k_{\alpha'_{\nu'},\nu'}\right\rangle. \tag{7}$$

In absence of deflated states, the effective Hamiltonian $\langle k_{\alpha,\nu}|\hat{H}|k_{\alpha',\nu'}\rangle$ is block tridiagonal with a maximum block size $2L+1$ and can be diagonalized easily, to evaluate the operator inverse. In contrast, the usual Lanczos recursion corresponds to the case $L = 1$: The block size is $2 \times 1 + 1 = 3$, which reflects the fact that only a single matrix element of the cluster Green's function can be evaluated per Krylov expansion.

The overall dimension of the generated Krylov subspace is given by NL, which amounts to $N-1$ applications of the Hamiltonian, and we refer to N as the Krylov order. This, however, comes at the cost of additional, global MPS arithmetics when reorthogonalizing the candidate states. The resulting approximations generally introduce instabilities in the band Lanczos recursion. Instabilities most prominently manifest in form of a loss of the block tridiagonal structure of the effective Hamiltonian. In other words, the weight of the basis states accumulates in the orthogonal complement of the targeted Krylov subspace.

The loss of accuracy of the Krylov subspace expansion leads in particular to two problematic issues. First, the loss of orthogonality among the basis states in the Krylov subspace cannot be completely compensated in practice: Due to the large number of basis states, a (full) reorthogonalization would not be efficient numerically. Second, a convergence criterion that relates error bounds of the cluster Green's function to the approximation quality of the Krylov subspace is required: Standard convergence criteria such as the relative change in the energy spectrum are numerically unstable. Our methodical developments target both convergence issues with the goal of a numerically stable band Lanczos recursion using MPS arithmetics that work at a finite, yet controlled approximation quality.

1. Energy truncation

Constructing Krylov spaces of higher order, an increasing number of highly excited states has to be captured by the MPS representations of the Krylov vectors. Unfortunately, states from the bulk of the many-body Hamiltonian's spectrum typically satisfy a volume law of entanglement [68] and are therefore the main reason for the exponentially increasing computational complexity. While this is a problem in general, here, we are interested in a faithful approximation of the poles of the Green's matrix, i.e., their positions and weights. Hence, we can exploit a strategy introduced previously in the context of expanding the resolvent in terms of Chebyshev polynomials [58]. The general idea is to construct local Krylov spaces at each lattice site and iteratively project the state's site tensors into a sequence of local Krylov subspaces. However, in contrast with projecting the site tensors into a certain energy window as described in Ref. [58], we use the local Krylov space expansion to construct a projector to the subspace containing the most relevant eigenstates, up to a defined threshold δ:

$$|\psi\rangle = \sum_n \underbrace{\langle \tilde{E}_n|\psi\rangle}_{\varepsilon_n} |\tilde{E}_n\rangle \approx \sum_{\varepsilon_n>\delta} \varepsilon_n |\tilde{E}_n\rangle, \tag{8}$$

where

$$|\tilde{E}_n\rangle = \sum_{l=0}^{K} c_l |v_l\rangle, \qquad \lim_{K\to\dim\mathcal{H}} \hat{H}|\tilde{E}_n\rangle = E_n|E_n\rangle, \tag{9}$$

and $|v_l\rangle \in \mathcal{H}_K$ Lanczos vectors in Krylov space $\mathcal{H}_K = \mathrm{span}\{|\psi\rangle, \hat{H}|\psi\rangle, \ldots, \hat{H}^K|\psi\rangle\}$. A schematic illustration of the energy truncation is shown in Fig. 1(a). The red shaded bars correspond to those eigenstates that have a weight $\langle \tilde{E}_n|\psi\rangle < \delta$ and are hence discarded. Referring to the expansion of the Green's function in the Krylov subspace (7), we can identify the weights with the expansion of the matrix elements $\langle k_{\alpha'_{\nu'},\nu'}|\hat{c}^\dagger_\mu|\psi\rangle$ in the energy eigenbasis. The energy truncation thus simply discards those eigenstates, whose contribution to the total Green's function are $O(\delta^2)$.

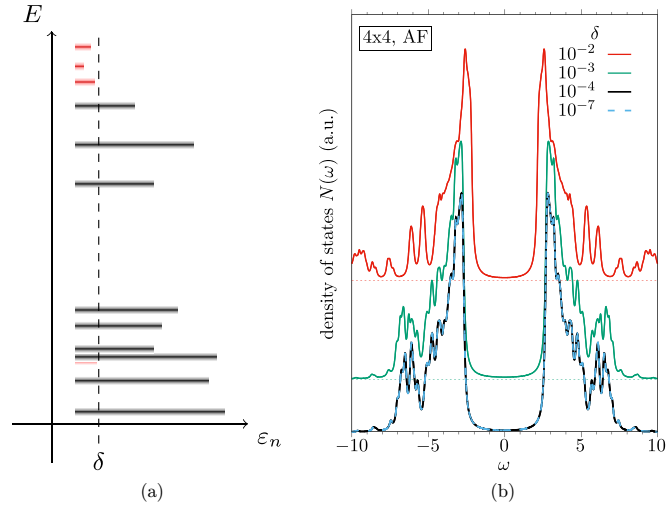


FIG. 1. (a) Schematic representation of the energy truncation. Overlaps $\epsilon_n = \langle \tilde{E}_n|\psi\rangle < \delta$ are neglected when constructing the sublattice projection (marked red). (b) Effect of the truncation threshold on the (lattice) density of states $N(\omega)$ for a 4×4 cluster in the AFM phase, see Sec. III B for details. The results for $\delta = 10^{-2}$, 10^{-3} are shifted for clarity.

In Fig. 1(b) we illustrate the effect of the energy truncation on the calculated lattice density of states (DOS) using the CPT Green's function for a 4×4 cluster in the antiferromagnetically ordered state. Setting the truncation threshold too high results in a breakdown of the subspace projection. Here, this is the case for $\delta = 10^{-2}$, where the erroneous subspace projection leads to a DOS, which neither captures correctly the gap nor the high-frequency part of the spectrum. However, already for moderate values of $\delta \lesssim 10^{-3}$ the spectrum is well reproduced, in particular the gap and the low-energy part of the spectrum, and only small deviations from the exact result are visible for higher excitation energies. A truncation threshold of $\delta \leqslant 10^{-4}$ finally leads to results which are for practical purposes essentially exact. In this case, only states with negligible weight for the density of states are truncated. The systematic improvements of the high-energy part of the spectrum can be related to the fact that the Green's function is computed from locally exciting the ground state, such that the weight of higher-energy eigenstates decreases rapidly. For the following calculations, we avoid any ambiguity by using an energy truncation threshold of $\delta = 10^{-5}$.

The computational costs of this energy truncation are not negligible. The complexity per local update scales as $O(Km^3wd) + O(Km^2w^2d^2)$, where K is the number of applications of the local representation of $\hat{H}$. Referring to standard notation, here we denote the MPS bond dimension by m, the MPO bond dimension by w, and the local Hilbert space dimension by d. Thus, we use the energy truncation only for the large clusters with $L \geqslant 16$ sites and apply it in the process of creating a new candidate state only once, namely, after the global application of $\hat{H}$. However, the goal is not to achieve a

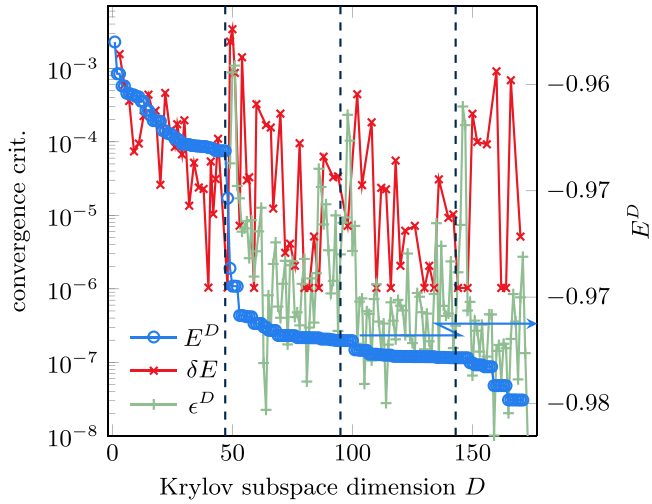


FIG. 2. Comparison of convergence criteria. The blue curve (right y axis) shows the lowest eigenvalue E^D of the effective Hamiltonian in the Krylov subspace as a function of the dimension D for a 4×6-site Hubbard cluster at $U = 8t$ and a staggered magnetic field $h_z = 0.09t$. The conventional convergence criterion $\delta E = E^{D+1} - E^D$ is given by the red line (left y axis), exhibiting strong fluctuations over several orders of magnitude. In contrast, oscillations in the suggested Hochbruck-Lubich criterion ϵ^D shown by the green line are significantly smaller, overlaying a systematic decrease with respect to the number of iterations.

speed up at constant m. Instead, we aim for a reduction of orthogonality losses that occur when orthogonalizing candidate states with respect to each other. Here, the effect of the energy truncation is to remove highly entangled contributions allowing for significantly higher precision in the orthogonalization procedure, while keeping the bond dimension fixed. We found that building up a reasonably large Krylov space of dimension $D \approx 100$ for the larger clusters using computationally feasible bond dimensions $m = 1024$–2048 was possible only when employing an energy truncation. Otherwise, orthogonality could not be maintained and the construction procedure would break down due to orthogonality losses.

2. *Hochbruck-Lubich criterion*

Controlling the convergence of the band Lanczos in the MPS representation is a suprisingly delicate problem. The unavoidable loss of numerical precision, caused by performing global operations using MPS arithmetics, as well as finite truncation errors, render standard convergence criteria such as the relative change in the ground-state energy in the constructed Krylov subspace not suitable. For instance, initially one observes a steep decrease of the relative error $\delta E = (E^{D+\alpha+1} - E^{D+\alpha})/E^{D+\alpha}$, where $E^{D+\alpha}$ is the ground-state energy after adding the αth candidate state to the Krylov subspace $\mathcal{K}_\sigma^D$. However, δE exhibits rather drastic jumps over more than an order of magnitude, paired with iterations where $\delta E = 0$ with respect to the energy resolution, which is bounded by the MPS truncation error. This phenomenon is shown at the example of a 4×6-Hubbard cluster in Fig. 2 where the red curves represent δE.

There are two major sources for an erroneous convergence indication in δE. First, whenever $\hat{H}$ is applied to a complete sequence of candidate states (here, $N \times 2L = N \times 48$ marked by the dashed lines), the Krylov order N increases. Given a fixed Krylov order, the band Lanczos generates a sequence of states that optimize the approximation of the ground state, which, however, is constraint by the Krylov order. Therefore, δE decreases within a sequence of candidate states, which leads to a false indication of overall convergence. Second, candidate states $|k_{\alpha,N}\rangle$ have a different relevance for the ground-state approximation. Most prominently, states that are created from initial excitations located at the boundary of the system converge more quickly.

Besides these technical problems, in practice the energy gain is not the most relevant quantity: In the end, the goal is to approximate the poles and weights of the cluster Green's function up to a certain precision. For that purpose, here we pursue a different approach using a convergence criterion that directly measures the desired approximation quality. The idea is to relate an error measure $\delta R^D(\tau)$, which can be derived for the approximation of the action of the operator exponential $\mathrm{e}^{-\mathrm{i}\hat{H}\tau}|\psi\rangle$ to the Green's function. Here, $\delta R^D(\tau)$ denotes the generalized residual introduced by Hochbruck and Lubich [39,69,70], which bounds the actual approximation error of the action of the operator exponential via $\delta R^D(\tau) \leqslant \epsilon^D$, and an estimation for ϵ^D is given by the Hochbruck-Lubich bound [39]

$$\epsilon_\tau^D \leqslant \frac{40}{\tau} e^{-\frac{\tau}{4}} \left(\frac{e\tau}{4D}\right)^D. \tag{10}$$

Note the exponential suppression of the bound on the time step τ. We propose to use the generalized residual for two reasons. (1) Evolving for small time steps τ, the approximation of the time evolution incorporates mostly low-lying excited states because the spread of information is limited by the Lieb-Robinson bounds [71] and $|\psi\rangle$ is close to the ground state. (2) $\delta R^D(\tau)$ is remarkably insensitive to small approximation errors in the low-energy spectrum, in particular if poles move close to each other in the scope of the Krylov sequence. In our computations, we choose $\epsilon \leqslant \delta R^D(\tau)$ as error threshold, which can be evaluated at negligible numerical costs from the matrix representation of the exponential of the effective Hamiltonian $\hat{H}^D$ [35,70] (see also Appendix B). We furthermore fix the time step by relating it to the spectral width W of $\hat{H}$ via $\tau = 2\pi/\kappa W$ where typically we choose the energy window fraction $\kappa \approx 1$.

We can now argue why we expect this error measure to be more reliable than only considering the relative change in the ground-state energy: $\delta R^D(\tau)$ is not a relative measure and while we also found it to exhibit fluctuations in our numerics, these are less severe than those in δE. The stability of $\delta R^D(\tau)$ against fluctuations comes from the fact that, increasing the Krylov space dimension D, the residual in approximating the time evolution is monotonically decreasing, which follows directly from Eq. (10). Thus, fluctuations can only be generated from approximation errors caused by the MPS arithmetics and truncation errors. The main effect of these errors is to destroy the block-tridiagonal form of the effective Hamiltonian, which, however, can be monitored by the precision of the MPS arithmetics and the truncation errors.

We choose the corresponding thresholds to be sufficiently small and thereby obtain a significantly more stable convergence criterion than using δE. It should be noted that, strictly speaking, Eq. (10) is valid only after a complete sequence of Lanczos states for the set of initial states $|\varphi^{(e)}_{j,\sigma}\rangle$ has been constructed, i.e., the Krylov space dimension has to fulfill $D = NL$. However, from our numerical experience we found that the violation of monotonicity while constructing a new set of L candidate states is not too severe.

3. Orthogonality loss

A major source for numerical instabilities in Krylov subspace methods is the loss of orthogonality of Krylov vectors. While in the commonly used exact state representations the loss of orthogonality is in general caused by round-off errors due to finite-precision arithmetics [72], the use of MPSs introduces additional error sources. On the one hand, generating a new set of candidate states in the Nth iteration of the band Lanczos recursion requires to act with the Hamiltonian on MPS representations of Lanczos vectors $|k_{\alpha,N}\rangle$: $|k_{\alpha,N}\rangle \longmapsto \hat{H}|k_{\alpha,N}\rangle$. Performing this operation by a naïve MPO-MPS application is numerically very costly so that we resort to a variational application scheme with a zipup preconditioner [35]. While this allows us to achieve convergence of the MPO application typically after two sweeps, we are still limited by the growth of the MPS bond dimension, requiring a finite truncated weight. On the other hand, the orthogonalization of new candidate vectors $\hat{H}|k_{\alpha,N}\rangle$ against previous Lanczos states has to be done using a variational update scheme at finite truncated weight, too. This introduces a further loss of numerical precision if the variational optimization can get stuck in local minima. We preconditioned the optimization using an optimized initial guess state generation by mixing small contribution of higher- and lower-order Krylov states into the candidates. Nevertheless, the band Lanczos recursion inevitably is going to loose orthogonality, and the rate at which this loss occurs crucially depends on the maximally allowed truncated weight.

To keep the recursions stable as long as possible, we exploit the energy truncation, which removes poles, i.e., eigenstates, with small weights in the Green's function from the Lanczos states. This truncation then allows us to use small truncated weights $\delta_{\text{trunc}} \sim O(10^{-10})$ at moderate bond dimensions. We typically allow for up to $\chi_{\max} = 1024$ states and only for large clusters increased that value, typically to $\chi_{\max} = 2048$ and in case of the 6×6 cluster shown in Sec. IV 3 up to $\chi_{\max} = 2560$. Throughout the band Lanczos recursion, we then monitor the violation of the anticommutation relations

$$\mathcal{I}_{j,\sigma;j',\sigma'} = \sum_{\alpha,\nu} \langle 0|\hat{c}^{\dagger}_{j,\sigma}|k_{\alpha,\nu}\rangle\langle k_{\alpha,\nu}|\hat{c}_{j',\sigma'}|0\rangle + \langle 0|\hat{c}_{j',\sigma'}|k_{\alpha,\nu}\rangle\langle k_{\alpha,\nu}|\hat{c}^{\dagger}_{j,\sigma}|0\rangle. \tag{11}$$

We consider a deviation

$$\delta_{\text{ol}} = \sqrt{\sum_{j,j'}\sum_{\sigma,\sigma'} \|\mathcal{I}_{j,\sigma;j',\sigma'} - \delta_{j,j'}\delta_{\sigma,\sigma'}\|^2} < 10^{-3}, \tag{12}$$

which is of the order of the total truncation error $\approx L\sqrt{\delta_{\text{trunc}}}$, as acceptable and terminate the Lanczos recursion if that threshold is exceeded. For all practical applications discussed in this paper, the energy truncation allowed us to perform $\approx O(100)$ Lanczos iterations without facing numerical instabilities caused by the orthogonality loss. Importantly, this number was sufficient to converge also the largest clusters and obtain faithful approximations of the relevant poles and weights of the cluster Green's function with respect to the convergence criterion introduced in Sec. III A 2.

4. Energy rescaling

To conveniently use the error bound (10) we always rescale the Hamiltonian such that the spectral width is given by $W \equiv 1$. Furthermore, the rescaling allows us to introduce another tool to control the quality of the constructed Krylov subspace. In fact, a severe loss of orthogonality in the band Lanczos is typically signalled by an artificial drop of the lowest eigenvalue $\tilde{E}^D_0$ of the effective Hamiltonian in the Krylov space $\mathcal{K}^D$ below the ground-state energy. For these reasons we rescale and shift the Hamiltonian $\hat{H}$ throughout our computations, which of course needs to be compensated for in the evaluation of the cluster Green's function. The first step of the rescaling is to obtain the spectral width

$$W = |E_0 - E_{\max}| \tag{13}$$

of $\hat{H}$ by calculating the ground-state energy E_0 and the energy of the highest excited state $E_{\max}$. Afterwards, the Hamiltonian is rescaled and shifted,

$$\hat{H} \to \hat{\tilde{H}} = \frac{\hat{H} - E_{\max}}{|E_0 - E_{\max}|}, \tag{14}$$

to force the spectrum to be located within the interval $[-1, 0]$. Thus, the lowest eigenvalue of the effective Hamiltonian serves as additional proxy to the convergence of the Krylov space by monitoring whether the condition $\tilde{E}^D_0 > -1$ holds true. We also note that, using the rescaled Hamiltonian, the Hochbruck-Lubich time step is related trivially to the energy window fraction $\tau = 2\pi/\kappa$.

B. VCA

The VCA [20] is an established quantum cluster technique, which is well-suited to probe correlated systems for symmetry-breaking fields [21,22]. It is based on the self-energy-functional (SEF) theory [73–75] and consists of determining the stationary points of the SEF $\Omega_{\mathbf{t}}[\mathbf{\Sigma}]$, which is related to the Baym-Kadanoff-Luttinger-Ward functional [76,77], with respect to trial self-energies of a reference system $\mathbf{\Sigma}(\mathbf{t}')$:

$$\Omega_{\mathbf{t}}[\mathbf{\Sigma}(\mathbf{t}')] = \Omega' + \operatorname{Tr}\ln\left(-\left[\mathbf{G}_0^{-1} - \mathbf{\Sigma}(\mathbf{t}')\right]^{-1}\right) - \operatorname{Tr}\ln(-\mathbf{G}'). \tag{15}$$

Here, $\operatorname{Tr}\mathbf{A} = T\sum_{\omega,\alpha} A_{\alpha,\alpha}(i\omega)$ at temperature T, Ω' denotes the grand potential, and $\mathbf{G}'$ the Green's function of the reference system. Since the theory requires the reference system to have the same interaction terms as the original system, the cluster self-energies can be varied via their one-body terms $\mathbf{t}'$. At a stationary point, the SEF represents an approximation of the grand potential of the original system in the

variational space of available self-energies of the reference system.

To investigate symmetry-broken phases, a (fictitious) symmetry-breaking Weiss field term can be added to the cluster Hamiltonian. The Weiss field strength is then one of the one-body terms, which are determined via the variational principle that leads to stationarity of the SEF with respect to the cluster self-energy.

Here, we focus on zero temperature, $T = 0$, and perform the summation over frequency ω_m in Eq. (15) analytically. In this case one obtains [23]

$$\mathrm{Tr}\ln\left(\mathbf{G}_0^{-1} - \mathbf{\Sigma}\right)^{-1} = \sum_m \omega_m \Theta(-\omega_m) - R, \tag{16}$$

$$\mathrm{Tr}\ln \mathbf{G}'^{-1} = \sum_m \omega'_m \Theta(-\omega'_m) - R, \tag{17}$$

with the Heaviside function $\Theta(\omega)$, a contribution R from the poles of the self-energy, the poles ω'_m of the cluster Green's function $\mathbf{G}'$, and the poles ω_m of the VCA Green's function $(\mathbf{G}_0^{-1} - \mathbf{\Sigma})^{-1}$. It is therefore useful to work with a Lehmann representation of the Green's function since it explicitly includes the information about its poles ω_m; for more details see Appendix A.

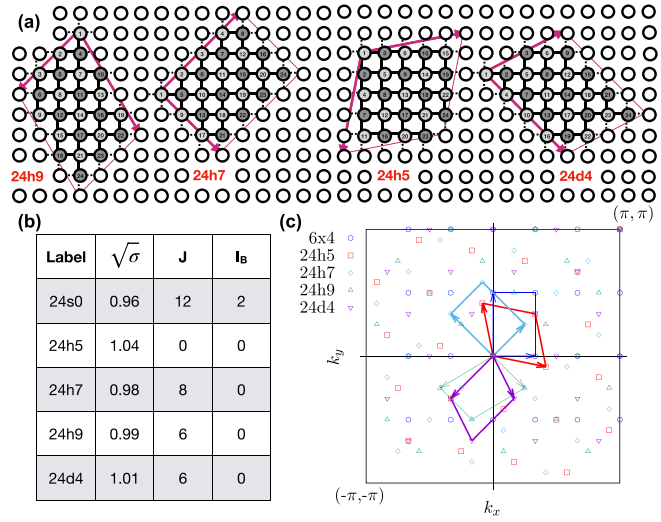
To limit the variational space of cluster self-energies, a limited set of one-body parameters of the cluster Hamiltonian are varied in practice: The hopping strengths $t_{ij}^{\mathrm{cluster}}$ can be determined from the variational principle to account for cluster-boundary effects [20], whereas the cluster chemical potential μ' should be optimized to obtain a thermodynamically stable electron filling n [78]. Additional one-body terms can be added to the cluster Hamiltonian to account for symmetry-broken phases such as magnetic order [21], superconductivity [22], or charge order [49].

In the half-filled 2D Hubbard model with isotropic nearest-neighbor hopping, the chemical potential is at $\mu = U/2$ and μ' does not need to be determined in the variational search. Furthermore it was shown that optimizing the cluster hopping terms did not lead to significant improvement of the approximation of the grand potential [20]. To capture the essential physics of AFM ordering, it is therefore sufficient to apply a staggered magnetic field of strength h_z on the cluster, see Eq. (3), and use it as the sole one-body parameter throughout the variational search.

C. Choice of clusters

The choice of a cluster is a centerpiece of most quantum cluster techniques, be it for accessing specific cluster momenta or for performing a finite-size scaling. Besides the size of the cluster, its geometry is of crucial importance in 2D systems and the seminal papers of Betts *et al.* [79,80] introduced a set of evaluation criteria for the suitability of clusters with periodic boundary conditions, which were based on the completeness of near-neighbor shells.

Within CPT and VCA one uses open boundary conditions on the clusters and a systematic study of Betts clusters is missing. Nevertheless, we resort here to the labeling and characterization scheme introduced by Betts *et al.* [79], in particular to parameters such as the geometrical imperfection J and the bipartite imperfection I_B to identify clusters of high geometrical and topological quality. Apart from more traditional rectangular clusters, we also test our solver on skewed Betts clusters. We limit ourselves to clusters that can tile bipartite lattices and focus on those which have zero bipartite imperfection. By combining calculations of several cluster geometries, we can access different points of the lattice Brillouin zone via reciprocal vectors of the superlattice. In Fig. 3 we illustrate this for lattice tilings using different 24-site clusters that fulfill the condition $I_B = 0$. Apart from the accessible wave vectors $\mathbf{k}$, the choice of the tiling also affects the complexity of the MPS calculation through the (optimized) mapping of the cluster sites onto a one-dimensional (1D) chain, which we discuss below.



Label	$\sqrt{\sigma}$	J	I_B
24s0	0.96	12	2
24h5	1.04	0	0
24h7	0.98	8	0
24h9	0.99	6	0
24d4	1.01	6	0

FIG. 3. (a) Illustration of the geometries of different clusters with $N = 24$ sites labeled according to *Betts et al.* [79]. Red arrows indicate the superlattice vectors that tile the lattice with the respective cluster, dashed lines indicate intercluster hopping terms and the Néel-type sublattice structure is indicated by different tones of gray. The clusters differ in their squareness σ, geometrical imperfection J, and bipartite imperfection I_B, see panel (b). (c) Points in the Brillouin zone that are multiples of reciprocal superlattice vectors, which are indicated by arrows. The corresponding reduced (superlattice) Brillouin zones are marked by parallelograms. An illustration of the corresponding one-dimensional mapping is shown in Appendix C.

IV. RESULTS AND DISCUSSION

In the following, we study the AFM ordering within the half-filled single-band Hubbard model to benchmark our solver. We focus here at the challenging point in parameter space $U/t = 8$, i.e., an on-site interaction equal to the bandwidth of the non-interacting dispersion, where the system is already in the Mott insulating regime.

Translated to the SEF, this leads to one stationary point, a maximum, at $h_z = 0$ corresponding to a nonmagnetic solution and to two minima at $h_z = \pm h_z^c \neq 0$ corresponding to a phase with AFM order, see Fig. 4. Since Ω is symmetric in h_z, we plot it in the following only for positive values of h_z. Compared with numerically exact solvers, the MPS-based solver introduces additional approximations, in particular since the MPS bond dimension is bound to a maximal value χ^{max} and

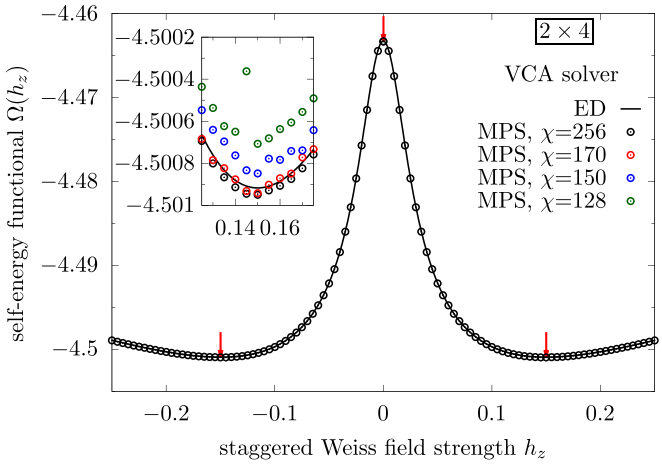


FIG. 4. The SEF Ω as a function of staggered Weiss field strength for a 2×4 cluster. Stationary points of Ω are indicated by arrows. Dots denote results obtained with the MPS-based solver, in the inset shown for different maximal MPS bond dimension $\chi^{\max}$ around the minimum of Ω; the results obtained with an ED solver are shown as a line.

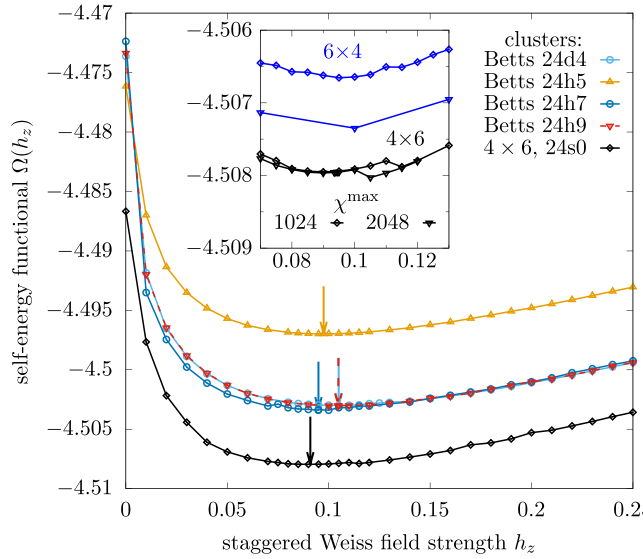


FIG. 5. Impact of the cluster geometry on the SEF. Ω is calculated with $\chi^{\max} = 1024$ for different 24-site clusters shown in Fig. 3. Minima of Ω are indicated by arrows, lines are only a guide to the eye. The inset shows Ω for two different 1D mappings of the 24s0 cluster, 4×6 and 6×4, calculated with $\chi^{\max} = 1024,\ 2048$.

since perfect orthogonality between the Krylov vectors is lost faster at large iteration numbers within the band Lanczos procedure. Comparing the SEF computed with our MPS-based solver to the benchmark using an ED-based solver, we see excellent agreement in Fig. 4 if the maximal MPS bond dimension is chosen large enough. For the small cluster used here, χ can be increased until the MPS representation is essentially exact. However, for too small bond dimension, deviations from the exact curve are visible. In that case, the SEF is systematically evaluated to be too large. Except for extreme cases, e.g., $\chi = 128$ in Fig. 4, Ω shows, even for moderate bond dimension, correct functional behavior as a function of the Weiss field, which allows for an interpolation around the stationary points. As we show in Sec. IV 1, fitting the SEF to determine its stationary points allows us to calculate observables for different bond dimension in order to perform an extrapolation to $\chi^{\max} \to \infty$.

To illustrate the effects of the cluster geometry on Ω, we plot in Fig. 5 the SEF of the 24-site clusters introduced in Fig. 3. Even though the rough functional forms of Ω do not differ qualitatively, their stationary points vary notably. We also note that clusters with similar geometric properties, such as, for instance, quantified in terms of their geometrical and bipartite imperfection, see Fig. 3(b), generate quite similar SEFs, whereas different imperfections of two clusters leads to significantly different Ω. Another consequence of using an MPS representation of the quantum states is that, even for a given cluster geometry, the obligatory mapping of the 2D cluster onto a 1D chain introduces a degree of freedom which has a direct impact on the precision with which the SEF is calculated. In the inset of Fig. 5 we illustrate this effect by calculating the cluster Green's function of the rectangular 24s0 cluster for two different 1D mappings. The corresponding SEFs agree in the $\chi \to \infty$ limit, but differ for finite χ. Whereas the mapping minimizing long-range hopping ("4×6") leads to well-converged results at $\chi^{\max} = 1024$, the longer-ranged mapping ("6×4") leads to a larger buildup of entanglement and would require a $\chi^{\max} > 2048$. The range of the hopping terms after a mapping to a 1D chain and the corresponding bipartite entanglement entropy of the ground state are discussed in Appendix C for the different 24-site clusters shown in Fig. 3.

In presence of nearly degenerate quantum states, different symmetry-breaking orders on the cluster can be easily picked up within MPS based approaches when not providing a sufficiently large bond dimension. This is, for instance, the case for the 4×6 mapped 24s0 cluster at $h_z \approx 0.11$, see inset of Fig. 5. Hence, scaling the position of the stationary points of Ω in the maximal MPS bond dimension instead of individual points of the SEF proved to be more robust.

1. SEF scaling with bond dimension

In Fig. 6, the value of the Weiss field h_z^c as well as the staggered magnetization on the lattice, $\langle m \rangle$, are scaled in the inverse bond dimension. It should be noted that other error bounds like the truncation error, which are well established for density-matrix renormalization group (DMRG) (ground state) calculations, are not applicable here since the calculation of the SEF using MPSs is not following an overall variational principle. For instance, the MPO application within the band Lanczos algorithm only allows us to estimate relative errors, and the propagation of these errors for the calculation of the SEF is not clear. Extrapolating the SEF in the inverse bond dimension therefore seems to be the most appropriate approach.

The staggered magnetization scales linear in $1/\chi^{\max}$ and gives a lower estimate of the expectation value for the $\chi^{\max} \to \infty$ limit. Since at some critical χ^c, the MPS representation is exact, we expect a constant value of $\langle m \rangle$ for $\chi^{\max} > \chi^c$. The value of $\langle m \rangle$ at the largest calculated $\chi^{\max}$

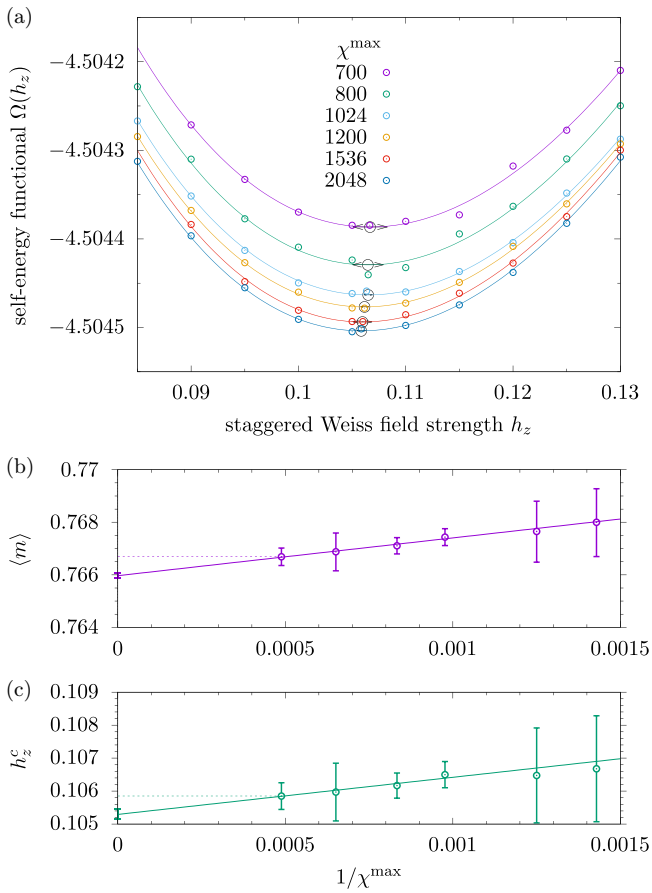


FIG. 6. Scaling of the SEF Ω in the maximal MPS bond dimension $\chi^{\max}$ for the Betts cluster 22h5. Around the stationary point $\Omega(h_z^c)$, the functional can be fitted as a function of the Weiss field, shown as a line in panel (a). The corresponding minima are indicated by black circles, the standard error of the minimum is indicated by black arrows. For different $\chi^{\max}$, the SEF shows similar functional dependence on h_z. (b) The staggered magnetization $\langle m \rangle$ on the lattice and (c) the Weiss field strength h_z^c are then scaled as a function of inverse bond dimension $1/\chi^{\max}$. We indicate both the standard deviation of the $1/\chi^{\max}$ extrapolated staggered magnetization as well as the value at the largest $\chi^{\max}$ (dashed lines).

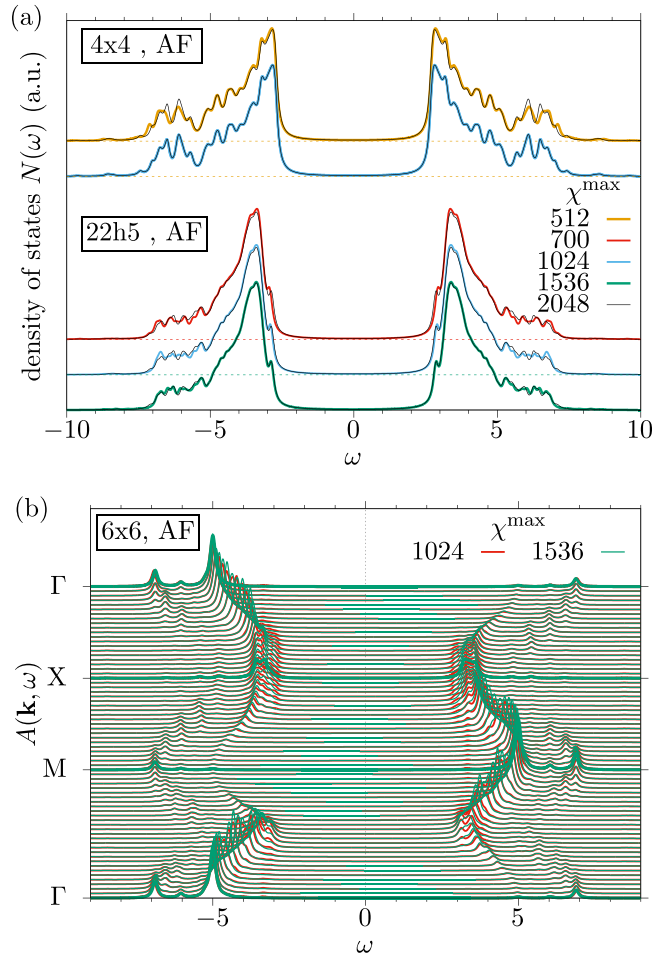


FIG. 7. (a) DOS $N(\omega)$ of the 4×4 (top) and 22h5 (bottom) clusters for different maximal MPS bond dimension $\chi^{\max}$. Panel (b) shows the **k**-resolved spectral function $A(\mathbf{k}, \omega)$ of a 6×6 cluster for two different maximal bond dimensions. All calculations were done in the AFM ordered state, i.e., at the stationary point of the SEF for the respective clusters.

therefore sets an upper bound for the staggered magnetization and can be used as a conservative upper error estimator.

However, the dependence of h_z^c and $\langle m \rangle$ on $1/\chi$ is mild $[O(10^{-3})]$ and of the same order as the estimated error such that it can be neglected in practice for most applications as long as a sufficiently large bond dimension χ is used. In the case of the shown 22-site Betts cluster, this would be the case for $\chi^{\max} \gtrsim 1000$. Given the large computational cost of evaluating the cluster Green's function via the MPS-based band Lanczos solver, systematically scaling expectation values in the MPS bond dimension should remain the exception. Instead, it offers the possibility to calculate spectral functions or observables for large clusters (e.g., using CPT), for which symmetry-breaking terms can be included via VCA. The rather mild dependence of the functional form of the SEF and the related expectation values on the chosen MPS bond dimension is important in this context.

2. *Spectral functions*

The spectral function defined via $A(\mathbf{k}, \omega) = -\frac{1}{\pi}\mathrm{Im}\mathbf{G}$ is commonly used to quantify the low-energy effective single-particle excitations, or more formally, it is the probability density to create a single-particle excitation with energy ω and momentum **k**. In particular, the single-particle dispersion relation $\varepsilon(\mathbf{k})$ and the DOS $N(\omega) = \sum_{\mathbf{k}} \delta(\omega - \varepsilon(\mathbf{k}))$ can be directly derived from $A(\mathbf{k}, \omega)$. Since it can be measured experimentally, for instance using angle-resolved photoemission spectroscopy (ARPES) [24,25], it constitutes an important quantity to establish effective model descriptions for real materials. As is usually done, we shift the Fermi momentum by choosing $\varepsilon_F = 0$ such that a vanishing spectral function in a finite region around $\omega = 0$ indicates the existence of a gap.

Next, we discuss the mild influence of the maximal MPS bond dimension $\chi^{\max}$ on the spectral function. In Fig. 7(a) we show the DOS and in Fig. 7(b) the spectral weight $A(\mathbf{k}, \omega)$

along a high-symmetry $\mathbf{k}$ path in the Brillouin zone. Since the dispersion of the model with nearest-neighbor hopping is particle-hole symmetric, we observe this symmetry also in the DOS. The chemical potential is located in the middle of the Mott gap, the system is hence Mott insulating, as expected for the half-filled Hubbard model in the strong-coupling regime.

For comparatively small clusters, the spectral function $A(\mathbf{k},\omega)$ and the DOS $N(\omega)$ can be converged in $\chi^{\max}$. We illustrate this in the case of the 4×4 cluster for $N(\omega)$ in Fig. 7(a). The results obtained from restricting the bond dimension to $\chi^{\max}=512$ show already good agreement for excitation energies close to the gap, but the DOS still shows differences at larger excitation energies around $\omega\approx\pm6$. For $\chi^{\max}\gtrsim1024$, the DOS and spectral function of the 4×4 cluster are converged and do not change any more upon increasing the bond dimension. We found this convergence of the Green's function (or the DOS), i.e., increasing the MPS bond dimension to better capture the high-frequency part, systematically throughout our simulations. It can be understood by noting that, in order to faithfully describe the large-ω regime one has to be able to describe higher excited states with high accuracy, which requires large Krylov subspace dimensions. However, constructing good approximations to Krylov vectors requires numerically-well-converged applications of $\hat{H}$ to previous Krylov vectors, a task that becomes increasingly complicated when it comes to the computation of higher-order Krylov vectors. In particular, the restricted bond dimension severely limits the approximation quality, which yields a degrading description of the high-energy behavior when decreasing the MPS bond dimension.

Unfortunately, the discarded weight, which typically constitutes a more explicit error measure in the context of MPS algorithms, cannot be used here. This is due to the fact that, when variationally evaluating the MPO-MPS application, i.e., minimizing the cost function $C=\|\hat{H}|\psi\rangle-|\varphi\rangle\|^2$ over all MPS representations $|\varphi\rangle$ with a maximum bond dimension χ, the absolute error C is unknown and only relative convergence within the sequence of site-tensor updates can be achieved [35]. As a consequence, it is not possible to relate the total error incurred due to a finite bond dimension, i.e., the discarded weight to the error of the MPO-MPS application.

For larger clusters like the $22h5$ cluster discussed previously in Fig. 6, scaling h_z^c and $\langle m\rangle$ still leads to minor changes when increasing the bond dimension up to $\chi^{\max}=2048$. However, tracking the changes of the DOS as a function of $\chi^{\max}$ reveals that only small changes close to the outmost band edges far from the gap are visible. The DOS for excitation energies $|\omega|\lesssim5$ is already converged for $\chi^{\max}=1536$ and even for $\chi^{\max}=1024$ the deviations from the converged solution are for most purposes negligible.

In Fig. 7(b) we finally show the $\mathbf{k}$-resolved spectral function $A(\mathbf{k},\omega)$ along the high-symmetry path $(0,0)$-$(\pi,0)$-(π,π)-$(0,0)$ for one of the largest clusters we systematically studied, the 6×6 cluster. The spectral function was calculated from the CPT Green's function, Eq. (2), using the periodization scheme proposed in Ref. [19]. In contrast with small and intermediate clusters, the SEF of the 6×6 cluster still shows notable differences as a function of the MPS bond dimension up to $\chi^{\max}=2048$. They translate to the spectral function in form of small differences in the low-energy excitations, most visible around the X point, $\mathbf{k}=(\pi,0)$. Nevertheless, the most salient features of the spectral function are already converged in the bond dimension for a remarkably small $\chi^{\max}=1536$. This can be seen as an advantageous feature of the MPS solver, which enforces due to the energy truncation scheme first the convergence of poles of the Green's function that contribute most spectral weight. The present MPS solver therefore even allows us to interpret spectral functions of large clusters for which a full convergence in terms of the MPS bond dimension cannot be achieved.

3. *Finite-size scaling*

To perform a finite-size scaling of the staggered magnetization, calculations need to be performed using different cluster sizes. However, even for fixed cluster size, the cluster geometry has an impact on the SEF since the corresponding cluster Green's functions include long-range correlations to a different extent. To include this information for the finite-size scaling, we use the quality factor introduced by Sénéchal in Ref. [82]. It amounts to comparing the intracluster hopping terms N_t^{cl} to the number of hopping terms per site in the infinite lattice and therefore takes into account both the cluster size and geometry. In the square lattice, this amounts to $q=N_t^{cl}/2L$. The scaling factor q thereby contrasts with other commonly used scaling parameters like $1-1/L$, which include only information of the cluster size.

When using this quality factor, the extrapolation of the Weiss field strength h_z^c to the thermodynamic limit leads to a vanishing field strength whereas the expectation value of the staggered magnetization on the lattice $\langle m\rangle$ extrapolates to a finite value, see Fig. 8(a). In the infinite-cluster-size limit, $q=1$, the symmetry-breaking field is not needed since the symmetry is spontaneously broken. There, the value of the staggered magnetization $\langle m\rangle|_{q=1}$ simply corresponds to the order parameter on the lattice. At half filling, $\langle m\rangle$ can be calculated numerically exactly using auxiliary-field quantum Monte Carlo (AFQMC) [83–88].

Comparing with the AFQMC result (dashed black line) of Seki and Sorella [81] we see that the linear scaling in q (dashed, violet graph) would lead to an overestimation by $\approx$20% of the staggered magnetization, i.e., the linear dependence $\langle m\rangle$ on q seems to hold only for small and intermediate cluster sizes. Indeed, for the largest clusters calculated with our MPS band Lanczos solver, we already observe a significant deviation from linear scaling (cf. the red highlighted symbols in Fig. 8). We believe that, besides others, the nonlinear q dependence is generated from the fact that in the presented calculations we did not vary the hopping amplitudes t_b at the cluster boundaries. In that case, an extrapolation would still be possible even though the exact functional dependency is unknown, and we propose a modified finite-size extrapolation procedure in the following.

Even though our VCA computations fixed potential variational parameters such as t_b, an extrapolation in the cluster size is still possible if we take into account that the variational parameters exhibit different functional dependencies with respect to the quality factor. For the antiferromagnetic Weiss field strength h_z^c, which mimics the effect of long-range order

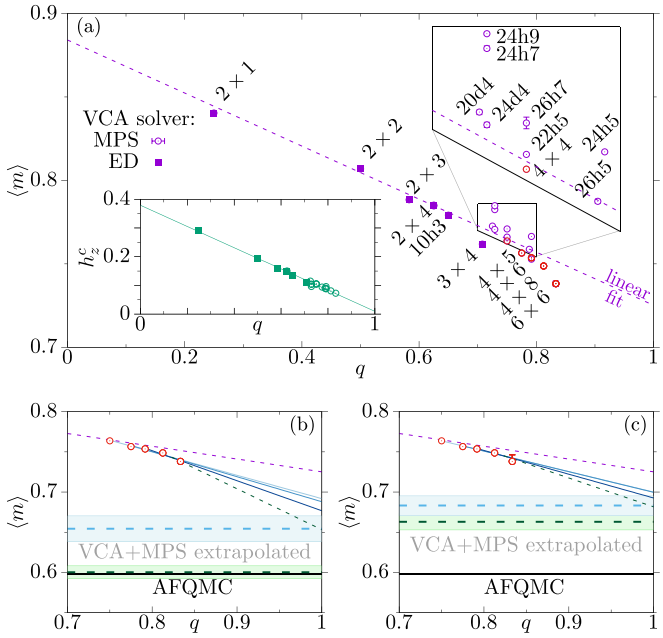


FIG. 8. Finite-size scaling of VCA data for different rectangular and Betts clusters. (a) The staggered magnetization $\langle m \rangle$ and the magnetic Weiss field on the cluster h_z (inset) are scaled as a function of the parameter q described in the text. The linear fit (violet dashed line) takes into account all data points, the band Lanczos results for large rectangular clusters (highlighted in red) are used in panels (b) and (c). (b) Extrapolation using a nonlinear ansatz as described in the text and based on the error estimate from the $1/\chi^{\max}$ extrapolation. The extrapolated staggered magnetization including (excluding) the last interpolation is shown as dashed green (blue) line, see text. We indicate the 1σ confidence interval of the extrapolation in light green (blue). (c) Same as panel (b) but with $m(\chi^{\max})$ as a conservative upper error estimate. In all cases, the linear extrapolation is improved with respect to the exact auxiliary-field quantum Monte Carlo result, taken from Ref. [81].

in the thermodynamic limit, a functional dependency of the form $h_z^c \sim 1 - L^{-1}$ is expected. This exactly corresponds to a scaling of the quality factor and is verified by our results as shown in the inset of Fig. 8. On the other hand, for the hopping amplitudes at the cluster boundaries, a functional dependency $t - t_b \sim 1 - L^{-1/2}$ could be expected, since the number of boundary sites of the square lattice scales as $L^{1/2}$. Assuming that the corrections $t - t_b$ vanish as $1 - L^{-1/2}$, these will dominate the magnetization for small q. Thereby, we can estimate the effect of fixing $t_b = t$ in our VCA computations by a rescaling of the otherwise linear dependency of the magnetization in q. We attempt to account for this nonlinear behavior by (1) Linearly extrapolating $\langle m \rangle(q \to 1, q_0)$ for the largest rectangular clusters (cf. the red highlighted symbols in Fig. 8) on a domain $[q_0, 1]$ where we varied $q_0 \in [0.775, 0.8125]$. The obtained linear extrapolations are indicated by the blue and dashed green lines in Figs. 8(b) and 8(c). (2) We then make the simplest nonlinear ansatz for the functional dependency on q_0:

$$\langle m \rangle(q \to 1, q_0) = \alpha(q_0 - 1)^2 + m_\infty. \tag{18}$$

TABLE I. Parameters of the low-energy effective models of $\delta = 0\%, 10\%$ hole-doped $CaCuO_2$, taken from Ref. [89].

δ	t (eV)	t'/t	$U/\lvert t\rvert$
0	−0.521	−0.21	8.60
0.1	−0.521	−0.25	8.10

This ansatz has a stationary point at $q_0 = 1$, resembling the expected asymptotic behavior of the magnetization when scaling the number of cluster sites to the thermodynamic limit. We extrapolate the data with (without) the last linear extrapolation ($q_0 = 0.8125$, green dashed line) and obtain the results shown in Fig. 8 as horizontal green (blue) dashed line. The corresponding 1σ confidence interval of the extrapolation is indicated by the shaded area. When including the $q_0 = 0.8125$ extrapolation, the extrapolated value $m_\infty = 0.602 \pm 0.008$ agrees with the AFQMC result $m_\infty^{\mathrm{QMC}} = 0.5982$ within the confidence interval.

A more conservative estimation of the extrapolation error can be obtained by taking the value $\langle m \rangle|_{\chi^{\max}=\max}$ as an upper error bound, see Fig. 8(c). In this case, the extrapolated magnetization $m_\infty = 0.663 \pm 0.010$ overestimates the exact value by 11% but still improves a linear-in-q fitting of all data.

We therefore find that, with the cluster sizes accessible via the VCA + MPS ansatz, it is possible to estimate values for local observables in the thermodynamic limit to a very high precision, even without exploring all possible variational parameters within VCA. As a final remark, we note that the constructed fitting procedure is only based on the fact that corrections in the order parameter generated by fixing variational parameters can exhibit different functional dependencies when scaling the system size. Thus, while this approach is generally applicable, it cannot establish absolute error bars, as long as the explicit extrapolation functions are unknown.

4. Application to hole-doped $CaCuO_2$

To illustrate the applicability of the MPS-based band Lanczos within VCA in situations where no (numerically) exact solutions exist, we employ it to the single-band Hubbard model away from half filling. Motivated by *ab initio* low-energy parametrizations of the "infinite-layer" cuprate $CaCuO_2$ at different levels of hole doping [89] we study here the $t - t' - U$ Hubbard model at densities between $n = 1$ and $n = 0.9$. $CaCuO_2$ has been in the focus over the last years, since it is isostructural to the nickelate $NdNiO_2$. The latter was recently synthesized hole-doped and found to show emergent superconductivity at low temperature [90].

Here, we slightly simplify the model given in Ref. [89] and use the parametrizations listed in Table I: We focus for undoped and hole-doped $CaCuO_2$ with $0 \leqslant \delta \leqslant 10\%$ on the parametrization for $\delta = 0$, at 10% doping we compare with the parametrization derived for $\delta = 0.1$. Longer-ranged hopping terms are rather small, which is why we focus here on the nearest- and next-nearest-neighbor hopping terms only, thereby neglecting hopping terms with $|t_i/t| < 0.11$. Furthermore, the nonlocal interaction terms $V_n/U < 0.25$ derived in

Ref. [89] are not included here, since they would require a mean-field decoupling at the cluster boundaries [49].

The full model has been studied recently with respect to its superconducting and AFM phases by employing a many-variable variational Monte Carlo technique based on variational wave functions on large square clusters [91]. However, the study did not comprise the calculation of quantities that rely on Green's functions such as the spectral function. Using a slightly different *ab initio* one-band model, the AFM phase of $CaCuO_2$ has also been studied by single-site DMFT [92] as well as with its cluster extension [93], which allows us to compare our results to techniques that include dynamical and—in case of cluster dynamical mean-field theory (C-DMFT)—also short-range spatial fluctuations.

Here, we focus on the AFM phase at and off half filling, thereby limiting the Weiss fields within VCA to a staggered magnetic field M_c and—in case of doping—to the cluster chemical potential μ'. We furthermore choose a chemical potential μ that optimizes the free-energy functional, thereby allowing for a thermodynamically stable electron density n [78]. To allow for commensurate electron fillings on the cluster at $\delta = 0.1$, we choose a 20-site cluster (4×5 or 20p0, see Fig. 9).

In Fig. 10(a) we show the evolution of the SEF upon hole doping. For the undoped system ($n = 1.0$), the SEF shows a minimum as a function of the Weiss field strength at $h_z \sim 0.08t$, which corresponds to an AFM insulator with staggered magnetization $\langle m \rangle = 0.377$. The value of the magnetization is in good agreement with the one reported in Ref. [93] from C-DMFT ($\langle m \rangle = -0.371$). This consistency could be expected since the correlations of an undoped Mott insulator in the strong-coupling region are short ranged such that both the 2×2 cluster and our 20-site cluster capture the correlations correctly. Upon doping, the minimum of the functional shifts continuously to smaller values of h_z and the condensation energy $F_{\mathrm{PM}} - F_{\mathrm{AFM}}$ reduces, finally leading to a transition to the nonmagnetic phase at $n \approx 0.9$. Comparing with the endpoint of the AFM solution in the finite-temperature phase diagram obtained within C-DMFT, we again find good agreement. Not surprisingly, the absence of dynamical and thermal fluctuations leads to a larger staggered magnetization close to the phase transition within VCA.

Having established the correct description of the AFM phase, we focus next on the spectral function at selected densities to exploit the good spatial resolution within our cluster approach. Figures 10(b) and 10(c) show the Fermi surface at $\delta = 2.5\%$ and $\delta = 10\%$ doping, respectively, as obtained from the periodized many-body Green's function, i.e., the spectral weight $A(\mathbf{k}, \omega)$ at $\omega = 0$. At low doping, the intensity close to the $(\pi, 0)$ and $(0, \pi)$ points disappears and only spectral weight around $\mathbf{k} = (\pi/2, \pi/2)$ is left. The absence of spectral weight at the nodal points while preserving spectral weight at the antinodal point is characteristic for hole-doped cuprates [94–96]. Here, we find a pronounced feature on the not-backfolded part of the spectrum, revealing Fermi arcs in contrast with Fermi pockets. Upon larger doping, nonzero spectral weight appears close to the noninteracting dispersion [Fig. 10(c)], finally showing a full Fermi sheet. These results are in good qualitative agreement with the Fermi surface obtained within C-DMFT on a 2×2 cluster [see Figs. 3(e) and 3(f) of Ref. [93]], even though the differences in cluster size lead to a richer structure of the Fermi surface at $\delta = 10\%$ within the VCA calculation on a 20-site cluster.

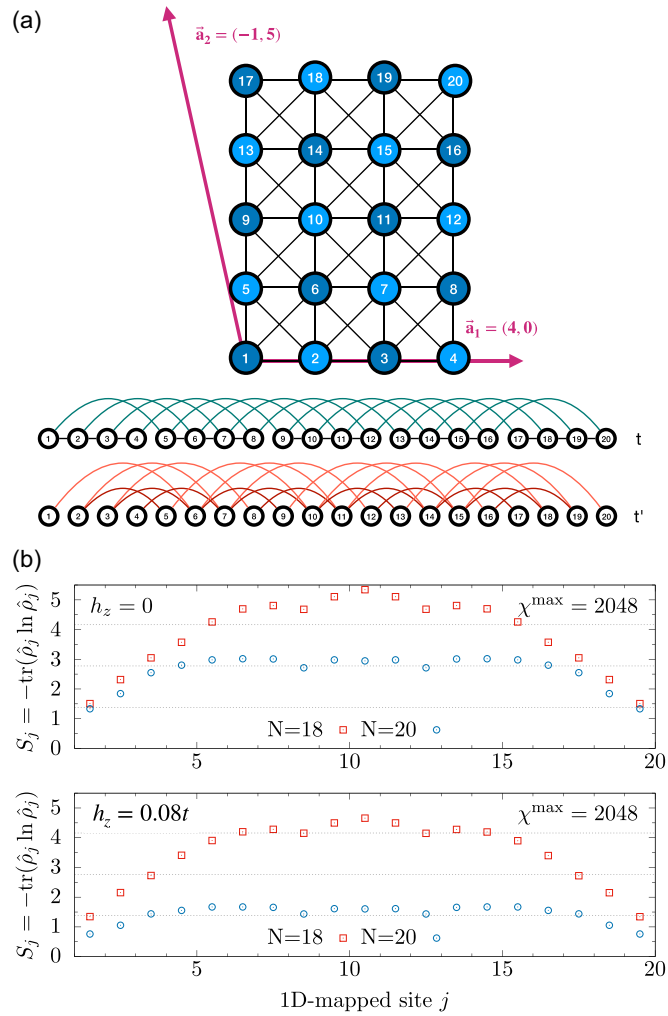


FIG. 9. (a) Cluster 20p0 used for the $t - t' - U$ Hubbard model (top) as well as its 1D mapping of the (next-)nearest-neighbor hopping terms (t') t (bottom). (b) Bipartite entanglement entropy S_j of the ground state wave function at Weiss field strengths of $h_z = 0$ (PM) and $h_z = 0.08t$ (AFM at half filling) for $N = 18$ and $N = 20$ electrons on the 20p0 cluster. The maximal MPS bond dimension is $\chi^{\max} = 2048$ and the dashed lines are a guide to the eye.

The larger spectral weight at the antinodal point and reduced weight along the remainder of the Fermi sheet are reminiscent of the strong-coupling pseudogap. This can be seen in Fig. 10(d), where the spectral function $A(\mathbf{k}, \omega)$ is shown along the high-symmetry $\mathbf{k}$ path Γ-M-X for the 10%-doped paramagnetic system: The Mott gap being located at positive energies 1.6 eV $\lesssim \omega \lesssim$ 3.6 eV as expected for electron-doped Mott insulators [97], the qualitative difference of the spectral weight at the Fermi level $\omega = 0$ along Γ-M and X-M is visible. In particular, at the antinodal point the peak of the spectral intensity does not coincide with the Fermi level, but a quasiparticle peak at ≈ -30 meV leads to the spectral weight at E_F. Here, no long-range AFM order is present ($h_z = 0$), but the 20-site cluster captures short-range

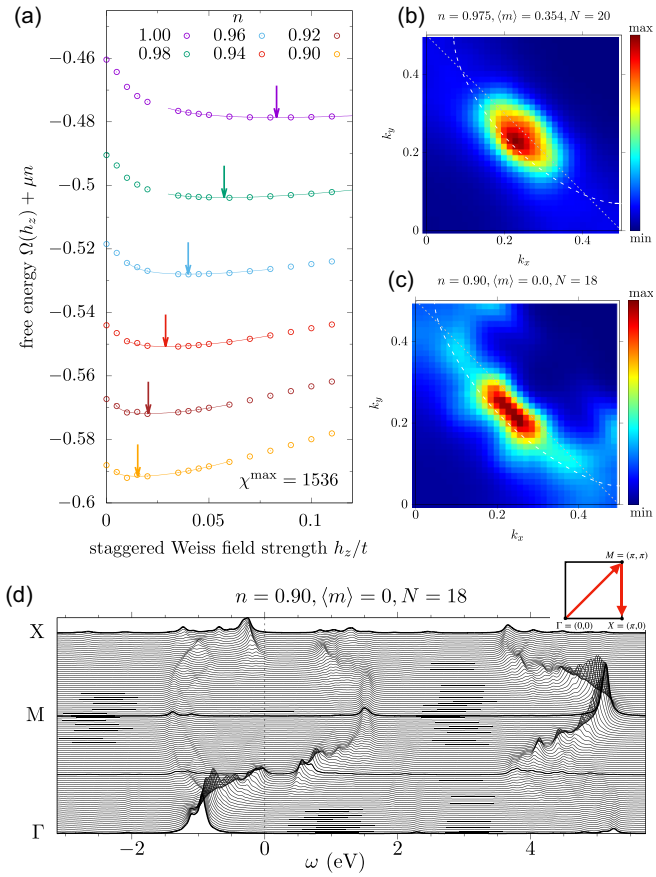


FIG. 10. VCA simulation of hole-doped and pristine $CaCuO_2$. (a) The SEF $\Omega(h_z) + \mu n$ with respect to the staggered Weiss field for different electronic densities n, limiting the quantum number sector on the cluster to $N = 20$ electrons. Lines indicate a fit around the minima, which are marked by arrows. The AFM solution can be stabilized for $1 \leqslant n \lesssim 0.9$. (b) First quadrant of the many-body Fermi surface in the AFM state at $n = 0.975$ (and $N = 20$) and (c) in the PM state at $n = 0.90$ for the $N = 18$ electron quantum sector. Dashed white lines indicate the noninteracting Fermi surface and the AFM BZ boundary is shown as a dashed gray line. $k_{x,y}$ are measured in units of 2π. (d) The single-particle spectral weight $A(\mathbf{k}, \omega)$ of the PM $\delta = 10\%$ doped system is shown for wave vectors along the high-symmetry directions shown in the bottom panel.

AFM fluctuations, which are known to cause the pseudogap formation in the strong-coupling regime of the Hubbard model [48,98].

Finally, we note that the description of the 10%-doped system within VCA is best done with a cluster that has a commensurate electron filling (i.e., $N = 18$ electrons on the 20-site cluster). In contrast with the half-filled cluster, this electronic configuration corresponding to a correlated metal with ungapped energy spectrum results in a higher bipartite entanglement entropy of the ground-state wave function, see Fig. 9. Whereas the presence of a finite staggered Weiss field h_z helps to reduce the bipartite entanglement entropy at half filling, the reduction is much smaller for the cluster with $N = 18$ electrons. Its description with MPS is therefore more challenging than the half-filled cluster. This is contrary to ED, where the dimension of the Hilbert space is the leading criterion for the numerical complexity, resulting in a numerically more challenging situation at half filling.

V. CONCLUSIONS AND OUTLOOK

We introduce a band Lanczos solver based on MPSs for quantum cluster methods such as the VCA. While a naïve implementation of MPSs as cluster solver does not lead to a substantial improvement over using ED techniques, we showed that significantly larger cluster sizes can be treated with high accuracy by combining the MPS + band Lanczos solver with a suitable energy truncation, controlling the loss of orthogonality of the Lanczos states and introducing a robust convergence criterion.

We demonstrate the potential of the approach by computing the staggered magnetization $\langle m \rangle$ of a single-band Hubbard model on a 2D square lattice. Treating different cluster sizes and shapes (regular rectangular as well as Betts clusters), we extrapolate our MPS data in the bond dimension χ, which we show to yield a systematic improvement of the approximation quality of the Green's function and its derived quantities. In this way we can exploit the increased number of accessible cluster sizes and geometries to extrapolate observables such as the staggered magnetization into the thermodynamic limit. We show that, at half filling and for intermediate interaction strengths $U/t = 8$ (i.e., in the Mott insulating regime, where the interaction strength is of the order of the bandwidth of the noninteracting system), an anomalous finite-size scaling with a crossover length scale is observed. Only for rectangular cluster sizes that are large enough, i.e., 4×4 and larger, a deviation from an otherwise linear scaling is obtained, which can be extrapolated toward the thermodynamic limit. The resulting value of $\langle m \rangle$ in the thermodynamic limit is improved over a simple linear-in-q extrapolation and can—depending on the extrapolation scheme—even agree within error margins with numerically exact QMC data. In contrast, with the smaller cluster sizes amenable to ED, the extrapolation in cluster size leads to a value, which overestimates the QMC result by $\approx$20%. We illustrate the applicability of the approach to more complex situations by studying the $t - t' - U$ Hubbard model at and off half filling as relevant to cuprate materials such as electron-doped $CaCuO_2$. The MPS-VCA ansatz allows us to study clusters with commensurate electron densities even at low electron doping.

Given the significant increase of the number of cluster sites, we envisage that our approach has the potential to substantially improve the investigations in multiband Hubbard-like models. Here, Hund's coupling leads to an interplay between orbital, spin, and electronic degrees of freedom [99,100], which affects material properties like superconductivity in nickelates and iron based superconductors, orbital selectivity in iron chalcogenides or optoelectronic and photovoltaic properties [90,101–107]. Although the interactions are local in nature, the higher complexity of these 2D systems poses an even stronger challenge to their theoretical description. While it is essentially impossible for ED-based solvers to treat cluster sizes large enough to perform meaningful studies on such multi-orbital systems, the MPS + band Lanczos approach makes it possible to treat also systems with larger local

Hilbert spaces in a controlled way so that it appears natural to extend our approach to such multiband situations.

ACKNOWLEDGMENTS

All MPS band Lanczos simulations were performed with the SYMMPS toolkit [108]. We thank the Grand Equipement National de Calcul Intensif for providing supercomputing time at IDRIS and TGCC (Project No. A0130912043). The authors gratefully acknowledge the computing time provided to them on the high performance computers noctua2 [109] at the NHR Center PC2. These are funded by the Federal Ministry of Education and Research and the state governments participating on the basis of the resolutions of the GWK for the national high-performance computing at universities [111]. We also acknowledge a mobility grant of the Franco-Bavarian University cooperation centre (BayFrance). Furthermore, funding through the ERC Starting Grant from the European Union's Horizon 2020 research and innovation programme under Grant Agreement No. 758935 is greatfully acknowledged. S.P. acknowledges support by the Deutsche Forschungsgemeinschaft (DFG, German Research Foundation) under Germany's Excellence Strategy-426 EXC-2111-390814868. Support by the Deutsche Forschungsgemeinschaft (DFG, German Research Foundation) - 207383564/FOR1807 project P7 at an early stage of this work is acknowledged.

APPENDIX A: *Q*-MATRIX FORMULATION OF THE CLUSTER GREEN'S FUNCTION

To rewrite the cluster Green's function, we use the **Q**-matrix formulation of the Lehmann representation introduced in Ref. [110]:

$$G'_{\alpha,\beta}(\omega) = \sum_m \frac{Q_{\alpha,m} Q^\dagger_{m,\beta}}{\omega - \omega'_m}, \tag{A1}$$

with α, β being compound site and spin indices, and excited states m. The **Q** matrix is defined as the concatenation of the electron and hole matrices

$$Q_{\alpha,m} = \left(Q^{(e)}_{\alpha,r}, Q^{(h)}_{\alpha,s}\right), \tag{A2}$$

$$Q^{(e)}_{\alpha,r} = \langle 0|\hat{c}_\alpha|r\rangle, \tag{A3}$$

$$Q^{(h)}_{\alpha,s} = \langle s|\hat{c}_\alpha|0\rangle, \tag{A4}$$

where $|0\rangle$ is the ground state with energy E_0. The corresponding excitation energies needed in Eq. (17) read $\omega'_m = (\omega^{(e)}_r, \omega^{(h)}_s) = (E_r - E_0, E_0 - E_s)$. To obtain the poles ω for Eq. (16) we rewrite the VCA Green's function as

$$\mathbf{G} = \frac{1}{\mathbf{G}_0^{-1} - \Sigma} = \frac{1}{(\mathbf{G}')^{-1} - \mathbf{V}} \tag{A5}$$

$$= \mathbf{Q} \frac{1}{\mathbf{g}^{-1} - \mathbf{Q}^\dagger \mathbf{V} \mathbf{Q}} \mathbf{Q}^\dagger, \tag{A6}$$

where $\mathbf{g}^{-1} = \omega - \mathbf{\Lambda}$ with $\Lambda_{m,l} = \delta_{m,l}\omega'_m$ so that the poles ω_m are nothing but the eigenvalues of $\mathbf{\Lambda} + \mathbf{Q}^\dagger \mathbf{V} \mathbf{Q}$. The **Q** matrix and the one-particle excitations ω' are calculated via the band Lanczos algorithm.

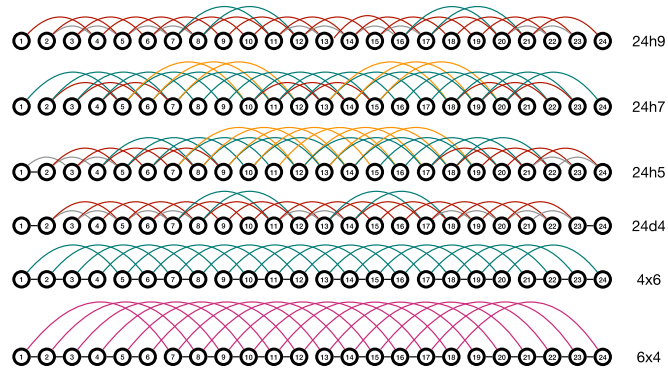


FIG. 11. 1D mapping of the 2D 24-site clusters discussed in the main text. The range of the hopping terms t_{ij} is illustrated by the height of the respective lines connecting two sites i and j.

APPENDIX B: GENERALIZED RESIDUAL

The generalized residual $\delta R^D(\tau)$ can be computed at no additional cost using the approximation of the exponential in the Krylov subspace

$$\delta R^D(\tau) = \beta^D \langle f^{D-1}|e^{-i\hat{H}^D\tau}|f^D\rangle. \tag{B1}$$

While this provides a reliable bound for the usual Lanczos procedure, Eq. (B.1) in the context of Eq. (10) is exact for the case of the band Lanczos only, if the Krylov dimension D and the Krylov order N, i.e., the number of applications of $\hat{H}$ to the set of L initial states, are related via $D = NL$. The reason behind this limitation is that deriving the Hochbruck-Lubich bound Eq. (10) for the generalized residual it is assumed that the residual Krylov vector $|f^D\rangle$ has a Krylov order $N+1$ while $\hat{H}^D$ is approximated with Krylov order N, only. In principle this means that Eq. (10) can only be applied after a whole sequence of L candidate states has been constructed. However, in practice we observed that also within such a sequence, the generalized residual $\delta R^D(\tau)$ yields satisfying error estimations with fluctuations being of an order of magnitude, at the most.

APPENDIX C: 1D MAPPING AND ENTANGLEMENT ENTROPY WITHIN MPS

Efficiently representing the Lanczos vectors in terms of MPS requires a certain care when choosing the mapping of the cluster geometry to a 1D chain. In particular, the computational efficiency and therefore also the achieved numerical accuracy given a fixed bond dimension χ crucially depends on the coupling ranges. This can be understood directly by noting that using MPS, two-point correlation functions are approximated by a sum of χ^2 exponentials [34]. Therefore, in choosing a specific chain mapping one should always try to minimize the coupling ranges in order to render correlations as short-ranged as possible to achieve a high approximation quality of the correlation functions. In Fig. 11, we show chain mappings for the various clusters computed in the main text and indicate the resulting couplings between the lattice sites of the chain. The bipartite entanglement entropy $S_j = \mathrm{tr}\,\hat{\rho}_j \ln \hat{\rho}_j$ constitutes a viable measure to quantify the range of correlations encoded in the MPS, where $\hat{\rho}_j$ denotes the reduced

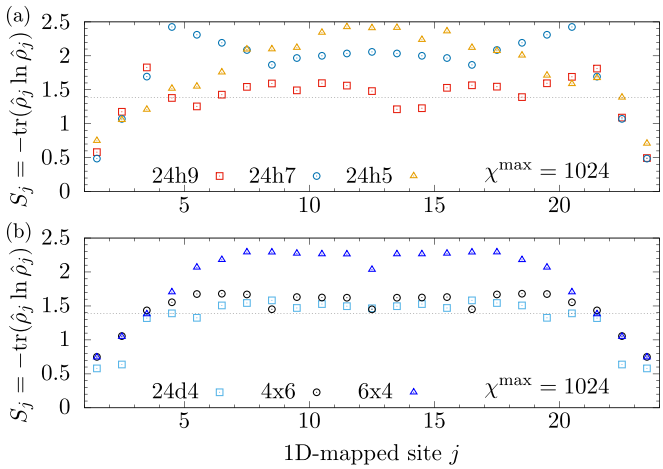


FIG. 12. The bipartite entanglement entropy $S_j = -\mathrm{tr}(\hat{\rho}_j \ln \hat{\rho}_j)$ of the ground state wave function of the 24-site clusters depicted in Fig. 11 for $\chi^{\max} = 1024$ at a Weiss field strength of $h_z = 0.10$.

density matrix when introducing a bipartition between sites $(j, j+1)$. For instance, considering a pair of maximally entangled (correlated) lattice sites the bipartite entanglement reaches its maximum value $S_0 = \ln d$ where d denotes the dimension of the local Hilbert spaces. For the case of a rectangular lattice with $L_x \times L_y$ sites mapped to a one-dimensional chain, one typically introduces a snake mapping, decomposing the system into either L_x or L_y coupled chains where the last site of the nth chain is connected to the first site of the $n+1$st chain. As a consequence, a bipartition between two sites can exhibit maximum values $S_{nL_{x,y}} = L_{x,y} \ln d$. It is therefore beneficial to decompose the grid in such a way that the length of the chains is minimized, i.e., for $L_x < L_y$ chains are formed along the x direction. We demonstrate this effect by computing the ground state of a 24-site cluster choosing both types of chain mappings for a rectangular cluster (4×6 and 6×4 sites where the first number denotes the length of the chains). In Fig. 12 we show the resulting bipartite entanglement entropies at the example of a maximum bond dimension $\chi = 1024$, demonstrating that, for chains with length 6, the maximally observed entanglement entropy is larger by a factor of roughly 1.5 compared with the case of chains with length 4. This illustrates how the size of the boundary determines the entanglement occurring in the MPS, which, in this case, nicely reproduces the area law of entanglement for ground states. For comparison, we also show bipartite entanglement entropies for various Betts clusters and we observe the largest values for the 24h5 cluster, which is consistent with large number of long-ranged couplings spanning six lattice sites.

[1] J. G. Bednorz and K. A. Müller, Possible high-T_c superconductivity in the Ba–La–Cu–O system, Z. Phys. B: Condens. Matter **64**, 189 (1986).

[2] E. Dagotto, Correlated electrons in high-temperature superconductors, Rev. Mod. Phys. **66**, 763 (1994).

[3] J. P. F. LeBlanc, A. E. Antipov, F. Becca, I. W. Bulik, G. K.-L. Chan, C.-M. Chung, Y. Deng, M. Ferrero, T. M. Henderson, C. A. Jiménez-Hoyos, E. Kozik, X.-W. Liu, A. J. Millis, N. V. Prokof'ev, M. Qin, G. E. Scuseria, H. Shi, B. V. Svistunov, L. F. Tocchio, I. S. Tupitsyn *et al.* (Simons Collaboration on the Many-Electron Problem), Solutions of the two-dimensional Hubbard model: Benchmarks and results from a wide range of numerical algorithms, Phys. Rev. X **5**, 041041 (2015).

[4] B.-X. Zheng, C.-M. Chung, P. Corboz, G. Ehlers, M.-P. Qin, R. M. Noack, H. Shi, S. R. White, S. Zhang, and G. K.-L. Chan, Stripe order in the underdoped region of the two-dimensional Hubbard model, Science **358**, 1155 (2017).

[5] Y. Cao, V. Fatemi, S. Fang, K. Watanabe, T. Taniguchi, E. Kaxiras, and P. Jarillo-Herrero, Unconventional superconductivity in magic-angle graphene superlattices, Nature (London) **556**, 43 (2018).

[6] X. Lu, P. Stepanov, W. Yang, M. Xie, M. A. Aamir, I. Das, C. Urgell, K. Watanabe, T. Taniguchi, G. Zhang, A. Bachtold, A. H. MacDonald, and D. K. Efetov, Superconductors, orbital magnets and correlated states in magic-angle bilayer graphene, Nature (London) **574**, 653 (2019).

[7] Y. Cao, D. Rodan-Legrain, O. Rubies-Bigorda, J. M. Park, K. Watanabe, T. Taniguchi, and P. Jarillo-Herrero, Tunable correlated states and spin-polarized phases in twisted bilayer–bilayer graphene, Nature (London) **583**, 215 (2020).

[8] S. Manzeli, D. Ovchinnikov, D. Pasquier, O. V. Yazyev, and A. Kis, 2D transition metal dichalcogenides, Nat. Rev. Mater. **2**, 17033 (2017).

[9] B. R. Ortiz, L. C. Gomes, J. R. Morey, M. Winiarski, M. Bordelon, J. S. Mangum, I. W. H. Oswald, J. A. Rodriguez-Rivera, J. R. Neilson, S. D. Wilson, E. Ertekin, T. M. McQueen, and E. S. Toberer, New kagome prototype materials: Discovery of KV_3Sb_5, RbV_3Sb_5, and CsV_3Sb_5, Phys. Rev. Mater. **3**, 094407 (2019).

[10] B. R. Ortiz, S. M. L. Teicher, Y. Hu, J. L. Zuo, P. M. Sarte, E. C. Schueller, A. M. M. Abeykoon, M. J. Krogstad, S. Rosenkranz, R. Osborn, R. Seshadri, L. Balents, J. He, and S. D. Wilson, CsV_3Sb_5: A $\mathbb{Z}_2$ topological kagome metal with a superconducting ground state, Phys. Rev. Lett. **125**, 247002 (2020).

[11] A. M. Seiler, F. R. Geisenhof, F. Winterer, K. Watanabe, T. Taniguchi, T. Xu, F. Zhang, and R. T. Weitz, Quantum cascade of correlated phases in trigonally warped bilayer graphene, Nature (London) **608**, 298 (2022).

[12] Z. Zhang, Z. Chen, Y. Zhou, Y. Yuan, S. Wang, J. Wang, H. Yang, C. An, L. Zhang, X. Zhu, Y. Zhou, X. Chen, J. Zhou, and Z. Yang, Pressure-induced reemergence of superconductivity in the topological kagome metal CsV_3Sb_5, Phys. Rev. B **103**, 224513 (2021).

[13] T. Neupert, M. M. Denner, J.-X. Yin, R. Thomale, and M. Z. Hasan, Charge order and superconductivity in kagome materials, Nat. Phys. **18**, 137 (2022).

[14] J.-X. Yin, B. Lian, and M. Z. Hasan, Topological kagome magnets and superconductors, Nature (London) **612**, 647 (2022).

[15] W. Metzner and D. Vollhardt, Correlated lattice fermions in $d = \infty$ dimensions, Phys. Rev. Lett. **62**, 324 (1989).

[16] A. Georges and G. Kotliar, Hubbard model in infinite dimensions, Phys. Rev. B **45**, 6479 (1992).

[17] A. Georges, G. Kotliar, W. Krauth, and M. J. Rozenberg, Dynamical mean-field theory of strongly correlated fermion systems and the limit of infinite dimensions, Rev. Mod. Phys. **68**, 13 (1996).

[18] C. Gros and R. Valentí, Cluster expansion for the self-energy: A simple many-body method for interpreting the photoemission spectra of correlated Fermi systems, Phys. Rev. B **48**, 418 (1993).

[19] D. Sénéchal, D. Perez, and M. Pioro-Ladrière, Spectral weight of the Hubbard model through cluster perturbation theory, Phys. Rev. Lett. **84**, 522 (2000).

[20] M. Potthoff, M. Aichhorn, and C. Dahnken, Variational cluster approach to correlated electron systems in low dimensions, Phys. Rev. Lett. **91**, 206402 (2003).

[21] C. Dahnken, M. Aichhorn, W. Hanke, E. Arrigoni, and M. Potthoff, Variational cluster approach to spontaneous symmetry breaking: The itinerant antiferromagnet in two dimensions, Phys. Rev. B **70**, 245110 (2004).

[22] D. Sénéchal, P.-L. Lavertu, M.-A. Marois, and A.-M. S. Tremblay, Competition between antiferromagnetism and superconductivity in High-T_c cuprates, Phys. Rev. Lett. **94**, 156404 (2005).

[23] M. Aichhorn, E. Arrigoni, M. Potthoff, and W. Hanke, Variational cluster approach to the Hubbard model: Phase-separation tendency and finite-size effects, Phys. Rev. B **74**, 235117 (2006).

[24] S. Hüfner, *Photoelectron Spectroscopy: Principles and Applications*, 3rd ed. (Springer Science & Business Media, Berlin, Heidelberg, New York, 2003).

[25] A. Damascelli, Z. Hussain, and Z.-X. Shen, Angle-resolved photoemission studies of the cuprate superconductors, Rev. Mod. Phys. **75**, 473 (2003).

[26] R. M. Noack and S. R. Manmana, Diagonalization- and numerical renormalization-group-based methods for interacting quantum systems, AIP Conf. Proc. **789**, 93 (2005).

[27] A. W. Sandvik, Computational studies of quantum spin systems, AIP Conf. Proc. **1297**, 135 (2010).

[28] J. I. Cirac and F. Verstraete, Renormalization and tensor product states in spin chains and lattices, J. Phys. A: Math. Theor. **42**, 504004 (2009).

[29] F. Verstraete, V. Murg, and J. I. Cirac, Matrix product states, projected entangled pair states, and variational renormalization group methods for quantum spin systems, Adv. Phys. **57**, 143 (2008).

[30] in *Quantum Simulations of Complex Many-Body Systems: From Theory to Algorithms*, edited by J. Grotendorst, D. Marx, and A. Muramatsu (John von Neumann Institute for Computing, Jülich, 2002).

[31] in *Quantum Monte Carlo Methods in Physics and Chemistry*, edited by M. P. Nightingale and C. J. Umrigar (NATO Science Series, 1999), Vol. 525.

[32] A. F. Albuquerque, F. Alet, P. Corboz, P. Dayal, A. Feiguin, S. Fuchs, L. Gamper, E. Gull, S. Gürtler, A. Honecker, R. Igarashi, M. Körner, A. Kozhevnikov, A. Läuchli, S. R. Manmana, M. Matsumoto, I. P. McCulloch, F. Michel, R. M. Noack, G. Pawlowski *et al.*, The ALPS project release 1.3: Open-source software for strongly correlated systems, J. Magn. Magn. Mater. **310**, 1187 (2007).

[33] A. Wietek and A. M. Läuchli, Sublattice coding algorithm and distributed memory parallelization for large-scale exact diagonalizations of quantum many-body systems, Phys. Rev. E **98**, 033309 (2018).

[34] U. Schollwöck, The density-matrix renormalization group in the age of matrix product states, Ann. Phys. (NY) **326**, 96 (2011).

[35] S. Paeckel, T. Köhler, A. Swoboda, S. R. Manmana, U. Schollwöck, and C. Hubig, Time-evolution methods for matrix-product states, Ann. Phys. (NY) **411**, 167998 (2019).

[36] F. Verstraete and J. I. Cirac, Renormalization algorithms for quantum-many body systems in two and higher dimensions, arXiv:cond-mat/0407066.

[37] M. Scheb and R. M. Noack, Finite projected entangled pair states for the Hubbard model, Phys. Rev. B **107**, 165112 (2023).

[38] M. Troyer and U.-J. Wiese, Computational complexity and fundamental limitations to fermionic quantum Monte Carlo simulations, Phys. Rev. Lett. **94**, 170201 (2005).

[39] M. Hochbruck and C. Lubich, Exponential integrators for quantum-classical molecular dynamics, BIT Numer. Math. **39**, 620 (1999).

[40] J. Hubbard, Electron correlations in narrow energy bands, Proc. R. Soc. London, Ser. A **276**, 238 (1963).

[41] S. Pairault, D. Sénéchal, and A.-M. S. Tremblay, Strong-Coupling expansion for the Hubbard model, Phys. Rev. Lett. **80**, 5389 (1998).

[42] D. Sénéchal, D. Perez, and D. Plouffe, Cluster perturbation theory for Hubbard models, Phys. Rev. B **66**, 075129 (2002).

[43] M. G. Zacher, R. Eder, E. Arrigoni, and W. Hanke, Stripes in doped antiferromagnets: single-particle spectral weight, Phys. Rev. Lett. **85**, 2585 (2000).

[44] A. S. Ovchinnikov, I. G. Bostrem, and Vl. E. Sinitsyn, Cluster perturbation theory for spin Hamiltonians, Theor. Math. Phys. **162**, 179 (2010).

[45] R. Eder, A. Dorneich, and H. Winter, Single-particle spectra of charge-transfer insulators by cluster perturbation theory: The correlated band structure of NiO, Phys. Rev. B **71**, 045105 (2005).

[46] C. Dahnken, E. Arrigoni, and W. Hanke, Spectral properties of high-T_c cuprates via a cluster-perturbation approach, J. Low Temp. Phys. **126**, 949 (2002).

[47] C. Dahnken, E. Arrigoni, W. Hanke, M. G. Zacher, and R. Eder, The cluster-perturbation-theory and its application to strongly-correlated materials, in *High Performance Computing in Science and Engineering, Munich 2002*, edited by S. Wagner, A. Bode, W. Hanke, and F. Durst (Springer, Berlin, Heidelberg, 2003), pp. 289–305.

[48] D. Sénéchal and A.-M. S. Tremblay, Hot spots and pseudogaps for hole- and electron-doped high-temperature superconductors, Phys. Rev. Lett. **92**, 126401 (2004).

[49] M. Aichhorn, H. G. Evertz, W. von der Linden, and M. Potthoff, Charge ordering in extended Hubbard models: Variational cluster approach, Phys. Rev. B **70**, 235107 (2004).

[50] M. Hohenadler, M. Aichhorn, and W. von der Linden, Spectral function of electron-phonon models by cluster perturbation theory, Phys. Rev. B **68**, 184304 (2003).

[51] M. Balzer and M. Potthoff, Nonequilibrium cluster perturbation theory, Phys. Rev. B **83**, 195132 (2011).

[52] V. I. Kuz'min, S. V. Nikolaev, M. M. Korshunov, and S. G. Ovchinnikov, One- and two-particle correlation functions in the cluster perturbation theory for cuprates, Materials **16**, 4640 (2023).

[53] N.-O. Linden, M. Zingl, C. Hubig, O. Parcollet, and U. Schollwöck, Imaginary-time matrix product state impurity solver in a real material calculation: Spin-orbit coupling in Sr_2RuO_4, Phys. Rev. B **101**, 041101(R) (2020).

[54] M. Ganahl, M. Aichhorn, H. G. Evertz, P. Thunström, K. Held, and F. Verstraete, Efficient DMFT impurity solver using real-time dynamics with matrix product states, Phys. Rev. B **92**, 155132 (2015).

[55] D. Bauernfeind, M. Zingl, R. Triebl, M. Aichhorn, and H. G. Evertz, Fork tensor-product states: Efficient multiorbital real-time DMFT solver, Phys. Rev. X **7**, 031013 (2017).

[56] M. Bramberger, B. Bacq-Labreuil, M. Grundner, S. Biermann, U. Schollwöck, S. Paeckel, and B. Lenz, Formation of CuO_2 sublattices by suppression of interlattice correlations in tetragonal CuO, SciPost Phys. **14**, 010 (2023).

[57] G. Bollmark, T. Köhler, L. Pizzino, Y. Yang, J. S. Hofmann, H. Shi, S. Zhang, T. Giamarchi, and A. Kantian, Solving 2D and 3D lattice models of correlated fermions—combining matrix product states with mean-field theory, Phys. Rev. X **13**, 011039 (2023).

[58] A. Holzner, A. Weichselbaum, I. P. McCulloch, U. Schollwöck, and J. von Delft, Chebyshev matrix product state approach for spectral functions, Phys. Rev. B **83**, 195115 (2011).

[59] A. C. Tiegel, S. R. Manmana, T. Pruschke, and A. Honecker, Matrix product state formulation of frequency-space dynamics at finite temperatures, Phys. Rev. B **90**, 060406(R) (2014).

[60] F. A. Wolf, I. P. McCulloch, O. Parcollet, and U. Schollwöck, Chebyshev matrix product state impurity solver for dynamical mean-field theory, Phys. Rev. B **90**, 115124 (2014).

[61] T. D. Kühner and S. R. White, Dynamical correlation functions using the density matrix renormalization group, Phys. Rev. B **60**, 335 (1999).

[62] A. Nocera and G. Alvarez, Root-N Krylov-space correction vectors for spectral functions with the density matrix renormalization group, Phys. Rev. B **106**, 205106 (2022).

[63] P. E. Dargel, A. Wöllert, A. Honecker, I. P. McCulloch, U. Schollwöck, and T. Pruschke, Lanczos algorithm with matrix product states for dynamical correlation functions, Phys. Rev. B **85**, 205119 (2012).

[64] H. D. Simon, The Lanczos algorithm with partial reorthogonalization, Math. Comput. **42**, 115 (1984).

[65] R. W. Freund, Band Lanczos method, in *Templates for the Solution of Algebraic Eigenvalue Problems: A Practical Guide*, edited by Z. Bai, J. D. Demmel, A. Ruhe, J. Dongarra, and H. van der Vorst (SIAM, Philadelphia, 2000), Chap. 4.6, pp. 80–88.

[66] T. E. Baker, A. Foley, and D. Sénéchal, Direct solution of multiple excitations in a matrix product state with block Lanczos, Eur. Phys. J. B **97**, 72 (2023).

[67] J. K. Cullum and R. A. Willoughby, *Lanczos Algorithms for Large Symmetric Eigenvalue Computations* (Society for Industrial and Applied Mathematics, 2002), https://epubs.siam.org/doi/pdf/10.1137/1.9780898719192.

[68] E. Bianchi, L. Hackl, M. Kieburg, M. Rigol, and L. Vidmar, Volume-law entanglement entropy of typical pure quantum states, PRX Quantum **3**, 030201 (2022).

[69] M. Hochbruck and C. Lubich, On Krylov subspace approximations to the matrix exponential operator, SIAM J. Numer. Anal. **34**, 1911 (1997).

[70] M. A. Botchev, V. Grimm, and M. Hochbruck, Residual, restarting, and Richardson iteration for the matrix exponential, SIAM J. Sci. Comput. **35**, A1376 (2013).

[71] B. Nachtergaele and R. Sims, Lieb-Robinson bounds and the exponential clustering theorem, Commun. Math. Phys. **265**, 119 (2006).

[72] G. Meurant and Z. Strakoš, The Lanczos and conjugate gradient algorithms in finite precision arithmetic, Acta Numerica **15**, 471 (2006).

[73] M. Potthoff, Self-energy-functional approach to systems of correlated electrons, Eur. Phys. J. B **32**, 429 (2003).

[74] M. Potthoff, Self-energy-functional approach: Analytical results and the Mott-Hubbard transition, Eur. Phys. J. B **36**, 335 (2003).

[75] M. Potthoff, Self-energy-functional theory, in *Strongly Correlated Systems: Theoretical Methods*, edited by A. Avella and F. Mancini (Springer, Berlin, Heidelberg, 2012), pp. 303–339.

[76] G. Baym and L. P. Kadanoff, Conservation laws and correlation functions, Phys. Rev. **124**, 287 (1961).

[77] J. M. Luttinger and J. C. Ward, Ground-state energy of a many-fermion system. II, Phys. Rev. **118**, 1417 (1960).

[78] M. Aichhorn, E. Arrigoni, M. Potthoff, and W. Hanke, Antiferromagnetic to superconducting phase transition in the hole- and electron-doped Hubbard model at zero temperature, Phys. Rev. B **74**, 024508 (2006).

[79] D. D. Betts, S. Masui, N. Vats, and G. E. Stewart, Improved finite-lattice method for estimating the zero-temperature properties of two-dimensional lattice models, Can. J. Phys. **74**, 54 (1996).

[80] D. D. Betts, H. Q. Lin, and J. S. Flynn, Improved finite-lattice estimates of the properties of two quantum spin models on the infinite square lattice, Can. J. Phys. **77**, 353 (1999).

[81] K. Seki and S. Sorella, Benchmark study of an auxiliary-field quantum Monte Carlo technique for the Hubbard model with shifted-discrete Hubbard-Stratonovich transformations, Phys. Rev. B **99**, 144407 (2019).

[82] D. Sénéchal, An introduction to quantum cluster methods, arXiv:0806.2690.

[83] J. E. Hirsch, Discrete Hubbard-Stratonovich transformation for fermion lattice models, Phys. Rev. B **28**, 4059 (1983).

[84] G. Sugiyama and S. E. Koonin, Auxiliary field Monte-Carlo for quantum many-body ground states, Ann. Phys. (NY) **168**, 1 (1986).

[85] S. Sorella, S. Baroni, R. Car, and M. Parrinello, A novel technique for the simulation of interacting fermion systems, Europhys. Lett. **8**, 663 (1989).

[86] M. Imada and Y. Hatsugai, Numerical studies on the Hubbard model and the t-J model in one- and two-dimensions, J. Phys. Soc. Jpn. **58**, 3752 (1989).

[87] N. Rom, D. M. Charutz, and D. Neuhauser, Shifted-contour auxiliary-field Monte Carlo: Circumventing the sign difficulty for electronic-structure calculations, Chem. Phys. Lett. **270**, 382 (1997).

[88] F. Becca and S. Sorella, *Quantum Monte Carlo Approaches for Correlated Systems* (Cambridge University Press, 2017).

[89] J.-B. Morée, M. Hirayama, M. T. Schmid, Y. Yamaji, and M. Imada, *Ab initio* low-energy effective Hamiltonians for the high-temperature superconducting cuprates $Bi_2Sr_2CuO_6$, $Bi_2Sr_2CaCu_2O_8$, $HgBa_2CuO_4$, and $CaCuO_2$, Phys. Rev. B **106**, 235150 (2022).

[90] D. Li, K. Lee, B. Y. Wang, M. Osada, S. Crossley, H. R. Lee, Y. Cui, Y. Hikita, and H. Y. Hwang, Superconductivity in an infinite-layer nickelate, Nature (London) **572**, 624 (2019).

[91] M. T. Schmid, J.-B. Morée, R. Kaneko, Y. Yamaji, and M. Imada, Superconductivity studied by solving *ab initio* low-energy effective Hamiltonians for carrier doped $CaCuO_2$, $Bi_2Sr_2CuO_6$, $Bi_2Sr_2CaCu_2O_8$, and $HgBa_2CuO_4$, Phys. Rev. X **13**, 041036 (2023).

[92] J. Karp, A. S. Botana, M. R. Norman, H. Park, M. Zingl, and A. Millis, Many-Body electronic structure of $NdNiO_2$ and $CaCuO_2$, Phys. Rev. X **10**, 021061 (2020).

[93] J. Karp, A. Hampel, and A. J. Millis, Superconductivity and antiferromagnetism in $NdNiO_2$ and $CaCuO_2$: A cluster DMFT study, Phys. Rev. B **105**, 205131 (2022).

[94] D. S. Marshall, D. S. Dessau, A. G. Loeser, C.-H. Park, A. Y. Matsuura, J. N. Eckstein, I. Bozovic, P. Fournier, A. Kapitulnik, W. E. Spicer, and Z.-X. Shen, Unconventional electronic structure evolution with Hole doping in $Bi_2Sr_2CaCu_2O_{8+\delta}$: Angle-resolved photoemission results, Phys. Rev. Lett. **76**, 4841 (1996).

[95] A. G. Loeser, Z.-X. Shen, D. S. Dessau, D. S. Marshall, C. H. Park, P. Fournier, and A. Kapitulnik, Excitation gap in the normal state of underdoped $Bi_2Sr_2CaCu_2O_{8+\delta}$, Science **273**, 325 (1996).

[96] H. Ding, T. Yokoya, J. C. Campuzano, T. Takahashi, M. Randeria, M. R. Norman, T. Mochiku, K. Kadowaki, and J. Giapintzakis, Spectroscopic evidence for a pseudogap in the normal state of underdoped high-T_c superconductors, Nature (London) **382**, 51 (1996).

[97] M. B. J. Meinders, H. Eskes, and G. A. Sawatzky, Spectral-weight transfer: Breakdown of low-energy-scale sum rules in correlated systems, Phys. Rev. B **48**, 3916 (1993).

[98] F. Šimkovic, R. Rossi, A. Georges, and M. Ferrero, Origin and fate of the pseudogap in the doped Hubbard model, Science **385**, eade9194 (2024).

[99] A. Georges, L. de' Medici, and J. Mravlje, Strong correlations from Hund's coupling, Annu. Rev. Condens. Matter Phys. **4**, 137 (2013).

[100] L. de' Medici, Hund's metals explained, in *The Physics of Correlated Insulators, Metals, and Superconductors*, edited by E. Pavarini, E. Koch, R. Scalettar, and R. Martin (Verlag des Forschungszentrum Jülich, Jülich, 2017), Chap. 14, pp. 377–398.

[101] N. Lanatà, H. U. R. Strand, G. Giovannetti, B. Hellsing, L. de' Medici, and M. Capone, Orbital selectivity in Hund's metals: The iron chalcogenides, Phys. Rev. B **87**, 045122 (2013).

[102] P. Villar Arribi and L. de' Medici, Hund's metal crossover and superconductivity in the 111 family of iron-based superconductors, Phys. Rev. B **104**, 125130 (2021).

[103] C. De Franco, L. F. Tocchio, and F. Becca, Metal-insulator transitions, superconductivity, and magnetism in the two-band Hubbard model, Phys. Rev. B **98**, 075117 (2018).

[104] A. Pham and S. Li, Engineering the strongly correlated properties of bulk Ruddlesden-Popper transition metal oxides via self-doping, Phys. Chem. Chem. Phys. **19**, 11373 (2017).

[105] M. Hepting, D. Li, C. J. Jia, H. Lu, E. Paris, Y. Tseng, X. Feng, M. Osada, E. Been, Y. Hikita, Y. D. Chuang, Z. Hussain, K. J. Zhou, A. Nag, M. Garcia-Fernandez, M. Rossi, H. Y. Huang, D. J. Huang, Z. X. Shen, T. Schmitt *et al.*, Electronic structure of the parent compound of superconducting infinite-layer nickelates, Nat. Mater. **19**, 381 (2020).

[106] M. Rahil, R. M. Ansari, C. Prakash, S. S. Islam, A. Dixit, and S. Ahmad, Ruddlesden–Popper 2D perovskites of type $(C_6H_9C_2H_4NH_3)_2(CH_3NH_3)_{n-1}Pb_nI_{3n+1}$ ($n = 1$–4) for optoelectronic applications, Sci. Rep. **12**, 2176 (2022).

[107] H. Tsai, W. Nie, J.-C. Blancon, C. C. Stoumpos, R. Asadpour, B. Harutyunyan, A. J. Neukirch, R. Verduzco, J. J. Crochet, S. Tretiak, L. Pedesseau, J. Even, M. A. Alam, G. Gupta, J. Lou, P. M. Ajayan, M. J. Bedzyk, M. G. Kanatzidis, and A. D. Mohite, High-efficiency two-dimensional Ruddlesden–Popper perovskite solar cells, Nature (London) **536**, 312 (2016).

[108] S. Paeckel and T. Köhler, SymMPS, https://www.symmps.eu, accessed: 2019-12-29.

[109] C. Bauer, T. Kenter, M. Lass, L. Mazur, M. Meyer, H. Nitsche, H. Riebler, R. Schade, M. Schwarz, N. Winnwa, A. Wiens, X. Wu, C. Plessl, and J. Simon, Noctua 2 Supercomputer, J. Large Scale Res. Facil. JLSRF **9** (2024).

[110] M. G. Zacher, R. Eder, E. Arrigoni, and W. Hanke, Evolution of the stripe phase as a function of doping from a theoretical analysis of angle-resolved photoemission data, Phys. Rev. B **65**, 045109 (2002).

[111] www.nhr-verein.de/unsere-partner.